Academic Year 2009/2010

Warsaw University of Technology
Faculty of Electronics and Information Technology
Electrical and Computer Engineering

MASTER OF SCIENCE THESIS

Dominik Mierzejewski

Roman Pot Detector Modelling and Proton Reconstruction in the TOTEM Experiment at the LHC

Supervisor
Janusz Rzeszut, PhD.

Evaluation: ....

....
Signature of the Head
of Examination Committee

Electrical and Computer Engineering

Date of Birth: 22 January 1979

Starting Date of Studies: 1 October 1998

Curriculum Vitae

I was born on 22 January 1979 in Olsztyn, Poland. In 1998, I graduated from the Catholic High School with distinction and was awarded the Primus Inter Pares award. Between 1998 and 2004, I studied at the Faculty of Electronics and Information Technology of the Warsaw University of Technology. In the years 1999-2000 I was granted a scholarship of the Faculty for the best students.
From 2000 to 2002 I worked at IDG Poland, S.A. as a Web and Database Programmer, where I was responsible for the maintenance and development of a web store and its database backend. There, I gained experience with technologies such as ASP, JavaScript, HTML and T-SQL. In the years 2003-2009, I worked as a System and Network Administrator at ICM, Warsaw University. My job involved maintaining the internal computer network, workstations and servers and ensuring smooth growth of the infrastructure. At ICM, I had an opportunity to manage Unix servers running Linux, Solaris and IRIX. Since 2009, I am a Software Engineer at the TOTEM experiment at CERN. My responsibilities include building detector geometry models using XML and simulation and analysis software development in C++ and Python.
Since 2004, I am a developer of the Fedora Linux distribution and I maintain a number of scientific software packages.

....
Signature of the Student

Master of Science Examination
Examination was held on: ....20__

With the result: ....

Final Result of the Studies: ....

Suggestions and Remarks of the M.Sc. Examination Committee: ....

....

....

SUMMARY

The objective of the TOTEM experiment at the LHC is the measurement of the total proton-proton cross-section with the luminosity-independent method based on the Optical Theorem, which requires studying both the elastic scattering cross-section and the inelastic (diffractive) processes. Movable insertions known as Roman Pot detectors provide the essential coverage of the high-rapidity region, enabling detection of forward protons at just a few millimetres from the beam centre. TOTEM software for simulation, reconstruction and analysis of both simulated and real event data relies on geometric models of the detectors and their surroundings to produce accurate and valid results. Precise computer model of the Roman Pot detectors geometry was developed in a Geant4-compatible way using XML-based Detector Description Language. Its accuracy was verified both visually and numerically. Finally, simulations of diffractive events were performed to validate its correctness.

Keywords: LHC, TOTEM, Roman Pot, detector model, DDL, XML, CSG

Modelowanie detektorów Roman Pot i rekonstrukcja protonów w eksperymencie TOTEM przy LHC

Celem eksperymentu TOTEM przy LHC jest pomiar całkowitego przekroju czynnego w zderzeniach proton-proton metodą niezależną od świetlności w oparciu o Twierdzenie Optyczne, co wymaga zbadania zarówno przekroju czynnego rozpraszania elastycznego, jak i procesów nieelastycznych (dyfrakcyjnych). Ruchome detektory zwane „Roman Pot” zapewniają niezbędne pokrycie regionu wysokiej pospieszności, umożliwiając wykrycie wiodących protonów w odległości zaledwie kilku milimetrów od środka wiązki. Oprogramowanie eksperymentu TOTEM do symulacji oraz rekonstrukcji i analizy danych zarówno symulowanych, jak i rzeczywistych potrzebuje modelu geometrycznego detektorów i ich otoczenia do uzyskania właściwych i dokładnych wyników. Precyzyjny model komputerowy geometrii detektorów Roman Pot został zaprojektowany i wykonany przy użyciu opartego o XML języka opisu detektorów (DDL) w sposób zgodny z Geant4. Jego dokładność została zweryfikowana zarówno wizualnie, jak i numerycznie. Dodatkowo, w celu zbadania jego poprawności, wykonane zostały symulacje zdarzeń dyfrakcyjnych.

Słowa kluczowe: LHC, TOTEM, Roman Pot, model detektora, DDL, XML, CSG

Contents

Abstract

The objective of the TOTEM experiment at the LHC is the measurement of the total proton-proton cross-section with the luminosity-independent method based on the Optical Theorem, which requires studying both the elastic scattering cross-section and the inelastic (diffractive) processes. Movable insertions known as Roman Pot detectors provide the essential coverage of the high-rapidity region, enabling detection of forward protons at just a few millimetres from the beam centre. Precise computer model of the Roman Pot detectors geometry, which is crucial to simulation and analysis of both simulated and real event data was developed. Its accuracy was verified both visually and numerically. Finally, simulations of diffractive events were performed to validate its correctness.

Chapter 1

Introduction

The TOTEM experiment at the LHC aims to measure the total proton-proton cross-section with the luminosity-independent method based on the Optical Theorem. To that end, both elastic and diffractive scattering processes have to be studied in detail, first in simulation and then with real data. The set of detectors designed for this task consists of two tracking telescopes T1 and T2 positioned close to the interaction point, used mainly for detection of diffractively scattered charged particles at large angles, and of Roman Pot detectors in movable insertions placed at distances of ± 147 m and ± 220 m from the interaction point mostly for detection of elastically scattered protons. The LHC and the TOTEM experiment are described in chapter 2.

TOTEM simulation and analysis software relies on the geometry model of the machine and the detectors to perform simulations of collisions and to reconstruct particle tracks from simulated or real events and analyse them. The software can use both ideal (design) geometry and real (misaligned) geometry, which is derived from the ideal one with the help of alignment procedures. Monte-Carlo simulations toolkit called Geant4 (chapter 3) is used for simulating the passage of particles through the detectors described by the geometry model in the software. TOTEM software is discussed in detail in chapter 4.

The correctness and the accuracy of the simulation and the subsequent analysis depends critically on having a precise model of the experimental apparatus, in this case — the LHC and the detectors of the TOTEM experiment. The objective of this work was the development of the precise model of the TOTEM experimental apparatus, reported in chapter 5.

TOTEM software was used to validate the model and the results of the validation are reported in chapter 6.

Chapter 2

TOTEM Experiment at the LHC

2.1 Purpose of the LHC

Ever since discovering that the atom is not an indivisible component of matter as its name would suggest, physicists have been trying to find the basic building blocks of matter and understand their interactions. The best description so far is the Standard Model, but it is still incomplete. The Large Hadron Collider (LHC) was built to help resolve some of the biggest unanswered questions of physics.

We have no explanation for mass. The question why some particles are so heavy while others have no mass at all remains unresolved. The Higgs boson, a hypothetical particle that is responsible for providing mass to other particles and might be the answer to the mass issue is a key but still unconfirmed element of the Standard Model. The LHC experiments ATLAS and CMS are trying to find confirmation of its existence.

All observed matter in the Universe accounts for only 4% of its estimated mass. The rest is theorised to consist of dark matter and dark energy, which are thought to be detectable only indirectly through their gravitational influence. A theory called Supersymmetry (SUSY) that postulates the existence of superheavy supersymmetric companions to all known particles could explain that phenomenon. If it is correct, then the ATLAS and CMS experiments should be able to detect the lightest supersymmetric particles.

Moments after the Big Bang, the conditions were too extreme for the components of atomic nuclei to exist. Instead, quarks, and the strong force mediators, gluons, floated freely in superdense quark-gluon plasma. As the Universe expanded, they combined, and should have formed matter and antimatter in equal amounts. This would have lead to a Universe filled with annihilation radiation and no matter at all. Obviously this hasn't happened and the only explanation is if laws of physics apply differently to matter and antimatter, i.e. if the CP[1] symmetry is broken. However, the Standard Model predictions either have not been experimentally confirmed yet or account for only a small portion of the CP violation. The LHCb experiment is studying the differences between matter and antimatter attempting to explain this imbalance. Another experiment, ALICE is using the LHC to recreate the conditions in which the quark-gluon plasma existed and study its properties.

String theories provide an alternative explanation for mass, proposing the existence of dimensions higher than four. These additional dimensions could be - according to the theories - detectable at extreme energies, which is why data from all experiments will be subjected to further analysis in search of indications that these hidden dimensions do exist.

2.1.1 The accelerator

There are two main types of particle accelerators: linear and circular (also known as particle storage rings). Linear accelerators consist of a straight pipe in which particles are accelerated using increasingly long magnets. The particles smash into stationary targets at the end of the pipe. Such machines are simpler to build, but the collision energy is very limited (it is proportional to the square root[2] of the accelerated particle energy). Circular colliders have significant advantages over others.

First, they can accelerate a particle as many times as necessary by passing it through the same magnets over and and over again, thus making use of the full potential of their circumference and magnetic field strength, which are the main limiting factors. Circular particle accelerators exploit the fact that a charged particle moving through a uniform magnetic field experiences a force (called Lorentz force) perpendicular to the directions of both the field and the motion of the particle. This force is expressed by the equation $F = qvB$, where q is the charge, v is the speed of the particle and B is the magnetic field. On the other hand, a centripetal force $F = \frac{mv^2}{r}$ is needed to keep a moving object on a circular trajectory. Consequently, a machine that maintains a magnetic field exerting a force equal to the necessary centripetal force is able to keep a charged particle in motion on a circular trajectory. For

[1] CP is the product of two symmetries: C for charge conjugation, which transforms a particle into its antiparticle, and P for parity, which creates the mirror image of a physical system.

[2] More precisely, the centre-of-mass energy in a collision of one stationary and one moving particle is proportional to the square root of the energy of the moving particle [1]

relativistic protons, the only variable parameters are therefore the radius of the trajectory and the magnetic field strength:

$$Br = \frac{mv}{q} = \frac{p}{q}, \tag{2.1}$$

where q is the charge of the particle. This means that to keep more energetic particles on a circular trajectory inside an accelerator, either a larger machine has to be built or a stronger magnetic field must be applied.

Second, the total collision energy is the sum [1] of the energies of two colliding particles. Unfortunately, circular accelerators have a disadvantage. Only charged particles (ions) can be accelerated using a magnetic field and ions moving along a curved trajectory emit electromagnetic radiation, losing energy. This radiation is known as the synchrotron radiation and must be compensated in the accelerator.

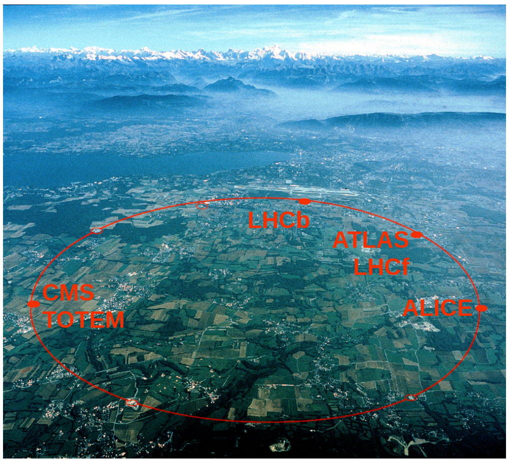

Figure 2.1: The LHC area overview. The names and locations of the experiments' detectors are shown.

The Large Hadron Collider (Figure 2.1) is not only the largest and most powerful particle accelerator in the world, but, with its 27 km circumference, also the largest machine ever built by humans. The LHC is designed to accelerate and collide two beams of protons or lead (Pb) ions rotating in opposite directions through the tunnel, which is located 50 to 175 meters underground on the French-Swiss border near Geneva. Centre of mass-energy of proton-proton collisions at the interaction point is expected to reach about 14TeV (7TeV per beam).

Particle accelerators are built with the purpose of studying physics processes which are difficult to reproduce because of their rarity or required energy. For physicists therefore, the most important parameters of an accelerator are the collision energy and the number of collisions. In particle storage ring-type accelerators like the LHC this relates to the parameter called luminosity, which depends on the number of particles circulating in the ring, the frequency of that circulation and the beam cross-section. In other words, it is necessary to squeeze the maximum number of particles into the smallest space at the crossing point and ensure the maximum number of crossings.

In an accelerator, particles move around through a vacuum pipe. Their trajectories are controlled using electromagnetic devices: dipole magnets to keep the particles in their nearly circular orbits, quadrupole magnets to focus the beam, and accelerating cavities (electromagnetic resonators) to accelerate particles and maintain their kinetic energy by compensating for energy losses due to synchrotron radiation.

In order to ensure that the hadrons interact only with their counterparts from the opposite beam, high vacuum is maintained inside the pipes. The pressure is below 10^{-9}bar.

The two counter-rotating beams consist of 7.48cm long cylinder-shaped bunches of $1.15 \cdot 10^{11}$ protons with 1mm^2 cross-section which gets reduced to $64\mu\text{m}^2$ at the Interaction Points (IPs). There is 7.5m spacing between the bunches, which - theoretically - allows 3550 bunches to be present in each beam. However, to allow space for bunch insertion and dumping, the number of bunches is reduced to 2808.

Even with such high number of protons in a bunch, the space per single proton is

$$7.48 \cdot 10^{-2}\text{m} \cdot 16 \cdot 10^{-6}\text{m} \cdot 16 \cdot 10^{-6}\text{m}/1.15 \cdot 10^{11} = 1.665 \cdot 10^{-4}\mu\text{m}^3,$$

which is much larger than an atom. Still, since the protons are accelerated to nearly the speed of light, it is possible to achieve a reasonable rate of interactions. Protons from opposite bunches collide with probability depending on proton size and bunch cross-section (which depends on accelerator optics):

$$P_{(p*p)} = d_p^2/\sigma^2 \Rightarrow P_{(p*p)} = (10^{-15})^2/(16 \cdot 10^{-6})^2 = 4 \cdot 10^{-21}.$$

Taking into account the number of protons in a bunch gives:

$$4 \cdot 10^{-21} \cdot (1.15 \cdot 10^{11})^2 = 45$$

potential collisions per every bunch crossing.

From the tunnel circumference and the speed of the protons we get the turn rate:

$$f = v/s \Rightarrow f = 299792455/26659 = 11245$$

laps per second.

Combining with the number of bunches, we get:

$$3550 \cdot 11245 = 40 \cdot 10^6$$

theoretical maximum crosses per second, which is why all data sampling equipment at the LHC operates at 40MHz. Of course, the real crossing rate is somewhat lower, namely

$$2808 \cdot 11245 = 31.6 \cdot 10^6.$$

Some of the more important parameters for the LHC are summarised in Table 2.1.

Quantity	Value
Circumference	26 659 m
Dipole operating temperature	1.9°K (-271.3°C)
Number of magnets	9593
Number of main dipoles	1232
Number of main quadrupoles	392
Number of RF cavities	8 per beam
Nominal energy, protons	7 TeV
Nominal energy, ions	2.76 TeV/u (*)
Peak magnetic dipole field	8.33 T
Min. distance between bunches	7 m
Design luminosity	$10^{34} cm^{-2} s^{-1}$
No. of bunches per proton beam	2808
No. of protons per bunch (at start)	$1.1 \cdot 10^{11}$
Number of turns per second	11 245
Number of collisions per second	600 million

Table 2.1: Basic LHC parameters. (*) Energy per nucleon

2.1.2 Accelerator optics

The LHC is divided into 8 sectors with eight straight and eight arc sections, shown in Figure 2.2. The straight sections (called insertions) are approximately 528m long. Some of them are used for physics experiments and the rest is designated for maintenance of the beam (insertion, cleaning and dumping). The arcs, connected to the insertions via transition regions (dispersion suppressors), consist of 23 cells housing six dipole magnets to deflect the particles and two quadrupole magnets to focus them (Figure 2.4).

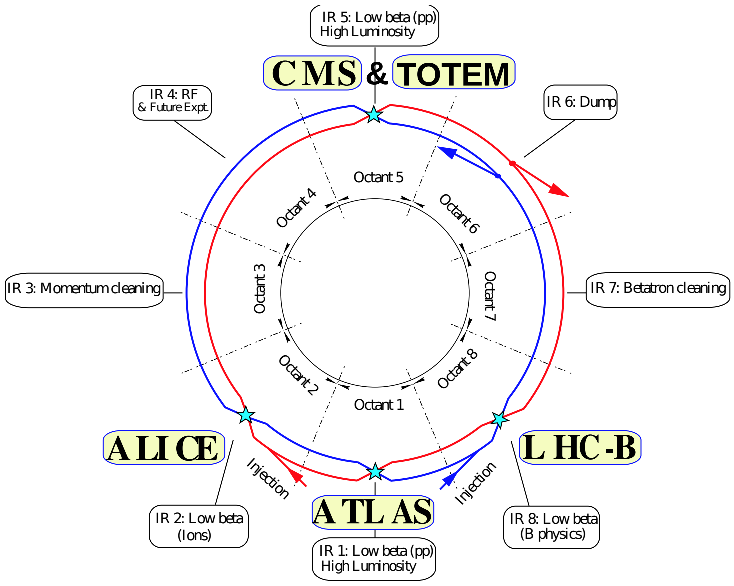

Figure 2.2: Sector layout of the LHC. Blue stars mark the four interaction points in the experimental halls where the counter-rotating beams cross each other.

The magnetic field of a vertically oriented dipole magnet causes the path of a charged particle to deviate by an angle in the horizontal plane, forcing a curved trajectory. The bending radius r, the bending magnetic field B and the momentum p of the beam particles, are related by the equation 2.1.

Particles travelling around the accelerator tunnel will follow different paths due to different initial angles and displacements as well as the gravity. If only dipoles affected their path, the particles would quickly fall outside the accelerator tunnel aperture, hence the need for beam focusing.

Quadrupoles are the primary focusing magnets in a storage ring-type accelerator. The property that makes them so useful is the shape of their magnetic field. Its strength is proportional to the distance from the central axis (which lies on the ideal particle trajectory), where it reaches zero. This configuration causes particles to be deflected towards the ideal trajectory in one plane (focusing effect) and away from it in the perpendicular plane (defocusing effect). The strength k of a quadrupole can be expressed by the gradient dB_y/dx of its magnetic field B_y normalised with respect to the magnetic rigidity Br:

$$k = \frac{1}{Br}\frac{\mathrm{d}B_y}{\mathrm{d}x}. \tag{2.2}$$

If the magnets are perfectly aligned, a proton with the correct energy and initial angle will pass through the centre of each quadrupole, following a central orbit around the synchrotron tunnel. Protons which deviate from the central axis in the horizontal plane are deflected back towards the centre of the magnet. In other words, the quadrupole magnet focuses the particles in the horizontal plane. However, the opposite is true in the vertical plane. Such magnet is called a Focusing Quad (QF). If we rotate this magnet by 90 degrees, it will become a Defocusing Quad (QD), which defocuses the particles in the horizontal plane, but focuses them in the vertical plane. A common combination of QF and QD magnets is the FODO lattice (shown in Figure 2.3), which consists of alternate focusing and defocusing sections

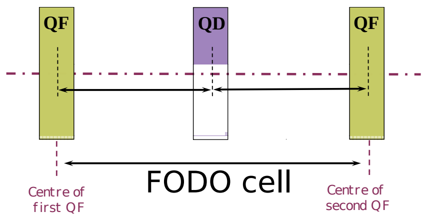

Figure 2.3: FODO lattice cell, consisting of alternating focusing (QF) and defocusing (QD) sections with drift sections in-between.

with non-focusing - drift sections between them. A variant of this lattice with additional small dipole, quadrupole, sextupole, octupole and decapole corrector magnets to keep the particles on stable trajectories is used in the LHC [2, 3] (Figure 2.4).

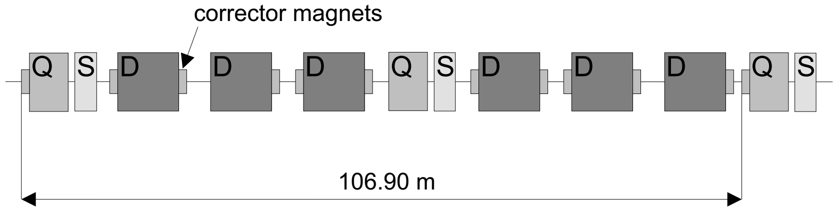

Figure 2.4: Schematic layout of an LHC arc cell. Main dipole (D), quadrupole (Q) and sextupole (S) magnets are shown. Small corrector magnets are also visible.

Equation of motion

Particles moving through an accelerator on non-ideal trajectories are subject to continuous focusing and defocusing by the quadrupole magnets, which causes them to oscillate in both horizontal and vertical planes. These are called betatron oscillations.

Let us consider their trajectories. The system of coordinates for a particle moving through an accelerator is shown in Figure 2.5. The s-coordinate

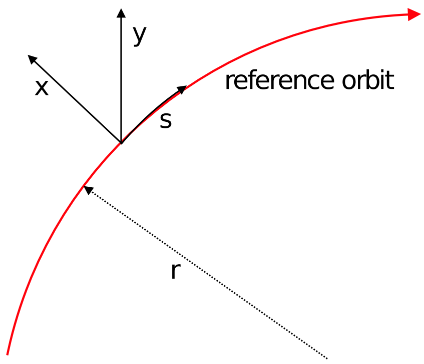

Figure 2.5: The system of coordinates for a particle motion in an accelerator. The particle follows a reference orbit s of (local) curvature r and is subject to transverse oscillations in the horizontal (x) and vertical (y) directions.

follows the ideal closed orbit (red line). The betatron oscillations cause displacements in the horizontal (x) and vertical (y) planes, perpendicular to the orbit. The particle trajectory may also have an angle with respect to the ideal orbit, which can be expressed as $\Theta_x \cong \frac{\mathrm{d}x}{\mathrm{d}s} = x'$ and $\Theta_y \cong \frac{\mathrm{d}y}{\mathrm{d}s} = y'$.

Without sacrificing generality, only the horizontal oscillations will be considered for simplicity. The angular divergence of a particle moving through a short quadrupole of length ds and strength k at a displacement dx is

$$\mathrm{d}x' = -kx\mathrm{d}s. \tag{2.3}$$

Taking into account that $k(s)$ is a function of the position s along the accelerator (due to the particle traversing magnets of varying properties), we get:

$$x'' + k(s)x = 0. \tag{2.4}$$

This is Hill's equation, the solution of which reads

$$x(s) = \sqrt{\beta_x(s)\varepsilon}\cos[\phi_x(s) + \phi_0], \tag{2.5}$$

where $\beta_x(s)$ is the betatron amplitude function, $\phi_x(s)$ is the phase advance of the oscillation of the particle, $\beta_x(s)$ is the amplitude the oscillation and ε is a constant. $\beta_x(s)$ is related to $\phi_x(s)$:

$$\frac{\mathrm{d}\phi_x}{\mathrm{d}s} = \frac{1}{\beta_x}. \tag{2.6}$$

Differentiating Equation 2.5 yields the angle of the particle in motion:

$$x' = -\sqrt{\frac{\varepsilon}{\beta_x(s)}}\sin[\phi_x(s)+\phi_0] + \left[\frac{\beta_x'(s)}{2}\right]\sqrt{\frac{\varepsilon}{\beta_x(s)}}\cos[\phi_x(s)+\phi_0]. \tag{2.7}$$

A plot of the equations 2.5 and 2.7 in the (x, x') phase space at any point along the accelerator results in an ellipse, whose shape varies depending on the location. Liouville's theorem [4] states that the area within the ellipse (equal $\pi\varepsilon$) is conserved. ε is the emittance of a beam of many particles and depends only on the initial conditions. Figure 2.6 illustrates the behaviour of the amplitude function β_x and the conservation of emittance of a beam

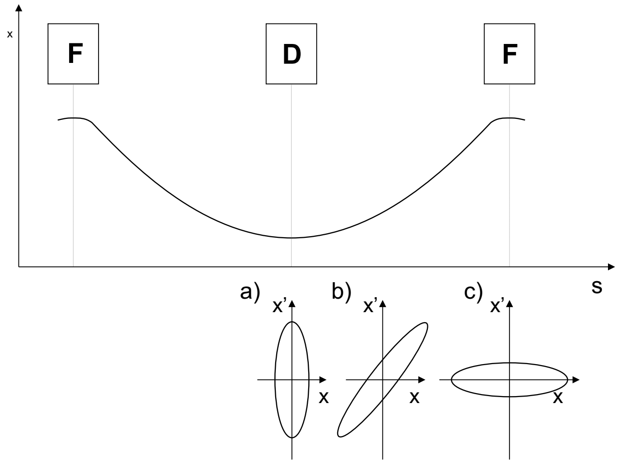

Figure 2.6: Changes in the shape of the beam phase space when crossing focusing (F) and defocusing (D) quadrupoles.

passing through FODO lattice. The amplitude function is at its minimum at the centre of a defocusing magnet (D), which corresponds to minimal beam size (a). At the centre of a focusing magnet (F), the beam size is at its maximum (c). The shape and orientation of the ellipse depend on the location, since β_x is a function of the position s, but its area remains constant.

The changes in beam size and divergence are represented by ellipses (a) – (c). Their horizontal and vertical projections are:

$$\Delta x = \pm\sqrt{\beta_x(s)\varepsilon} \quad \text{and} \quad \Delta x' = \pm\sqrt{\frac{\varepsilon}{\beta_x(s)}}\sqrt{1+\left(\frac{\beta_x'(s)}{2}\right)^2}. \tag{2.8}$$

At the centres of the focusing magnets, where β_x is at an extremum, β_x' becomes 0 and the equations can be simplified, because the correlation between particle displacement and divergence disappears. This allows the beam size and divergence to be expressed in terms of the beam emittance ε and the betatron amplitude $\beta_x(s)$:

$$\sigma(x) = \sqrt{\varepsilon\beta_x}, \tag{2.9}$$

$$\sigma(x') = \sqrt{\frac{\varepsilon}{\beta_x}}. \tag{2.10}$$

The emittance ε is conserved only if the particle(s) energy remains constant. A beam with varying energy must be described with so-called normalised emittance

$$\varepsilon_N = (\beta\gamma)\varepsilon, \tag{2.11}$$

where $\beta = \frac{v}{c}$, v is the velocity of the particle, c is the speed of light and $\gamma = \frac{1}{\sqrt{1-\beta^2}}$ is the Lorentz factor. The parameter β of Equation 2.11 should not be confused with the amplitude function used for example in Equation 2.5. Considering equation 2.6, the phase advance $\Delta\phi$ during one turn of the particle can be defined as:

$$\Delta\phi = \oint \frac{\mathrm{d}s}{\beta(s)}. \tag{2.12}$$

The number of oscillations of a particle in one turn around the accelerator is called the betatron tune and is defined as:

$$Q = \frac{\Delta\phi}{2\pi}. \tag{2.13}$$

The horizontal (Q_x) and vertical (Q_y) tunes are crucial in accelerator design due to the dependence of the beam stability on their values. Their values must be chosen so that the particles does not follow the same trajectory around the ring each turn. This is necessary to avoid the amplification of the side-effects (for example, resonances) of the imperfections of the magnets. In general, the relation $n \cdot Q_x + m \cdot Q_y = k$ should not be true (k, m, and n being integers). The betatron tunes of the LHC are around 60 and can be adjusted with quadrupole corrector magnets.

Beam transport matrix

The transverse position and the angle of a particle at some point along an accelerator can be represented by a column matrix $\binom{x}{x'}$, which will vary as the particle traverses the various magnets and drift spaces. These changes can be expressed in terms of a transport matrix. Movement of a particle from one point (s_1) to another (s_2), can be therefore written as:

$$\begin{pmatrix} x_{s_2} \\ x'_{s_2} \end{pmatrix} = \begin{pmatrix} a & b \\ c & d \end{pmatrix} \begin{pmatrix} x_{s_1} \\ x'_{s_1} \end{pmatrix} = M \begin{pmatrix} x_{s_1} \\ x'_{s_1} \end{pmatrix} \tag{2.14}$$

Coefficients a and b are especially interesting, because they determine the transverse displacement of the particles moving between points s_1 and s_2. This can be used to calculate the hit positions on detectors for particles emerging from the interaction point. In general, a and b can be treated as functions of s and they are called the optical functions. The parameter $a(s)$ is called magnification $v_x(s)$ and $b(s)$ is the effective length — $L_x(s)$.

Components of the matrix M and the amplitude β and phase ϕ of the transverse motion between points s_1 and s_2 are related. Their values can be derived from Equations 2.5 and 2.7 — the details can be found in [3]. The matrix M can be calculated as a product of the elementary transport matrices corresponding to all elements and sections of the accelerator. This is very similar to the transport of light through a system of lenses. For example, a straight drift section of length l is described by the matrix

$$M_d = \begin{pmatrix} 1 & l \\ 0 & 1 \end{pmatrix}. \tag{2.15}$$

A thin quadrupole magnet of infinitely small length l but finite magnetic field gradient is represented by

$$M_q = \begin{pmatrix} 1 & 0 \\ -kl & 1 \end{pmatrix}, \tag{2.16}$$

where k is defined by Equation 2.2. Defining $kl = \frac{1}{f}$, we get the same matrix as a thin optical lens with focal length f has:

$$M_q = \begin{pmatrix} 1 & 0 \\ -\frac{1}{f} & 1 \end{pmatrix}. \tag{2.17}$$

The magnetic lenses of a real accelerator are not normally short compared to their focal length which results in a more complex form of transport matrices than that presented in Equation 2.16, but it is possible to calculate the transport matrix between any two arbitrary points along the accelerator. Obviously such calculations are too complicated to be performed manually, so accelerator design is performed with computer programmes, which include in their routines all the matrix multiplications (for example, MAD-X [5]).

Dispersion and chromaticity

The bending magnets of an accelerator are designed for beams of particles of equal momentum p. Such particles, when injected into the central axis would follow the ideal central trajector along the accelerator.

However, in reality, the particles in the beam will have slight differences from the nominal momentum. For example, if a particle with a lower momentum $p = p_n - \Delta p$ travels through a dipole magnet, it is deflected by a larger angle than the particle with the nominal momentum p_n. This difference is compensated by the quadrupole magnets and the off-momentum particle follows another, but still closed orbit. This new orbit can be described by the dispersion function D(s). The dispersion effect for off-momentum orbits is cumulative with betatron motion. The horizontal coordinate of the resulting transverse particle motion is then:

$$x(s) = \sqrt{\beta_x(s)\varepsilon}\cos[\phi_x(s) + \phi_{x0}] + D(s)\xi, \tag{2.18}$$

where $\xi = \frac{\Delta p}{p}$ and Δp is the momentum difference. Obviously, a beam with momentum spread will be wider. If $\sigma(x)$ is the beam size resulting only from betatron oscillations and assuming the momentum distribution and betatron oscillations are independent, the full beam size becomes:

$$\sigma_D(x) = \sqrt{\sigma(x)^2 + \left(D_x \frac{\sigma(p)}{p}\right)^2}, \tag{2.19}$$

where $\sigma(p)$ is the RMS of the momentum spread and p is the nominal beam momentum.

After including the effect of the dispersion (by adding a ξ term), the beam transport matrix becomes a 3×3 matrix:

$$\begin{pmatrix} x_{s_2} \\ x'_{s_2} \\ \xi \end{pmatrix} = \begin{pmatrix} a & b & D_x \\ c & d & m_{23} \\ 0 & 0 & 1 \end{pmatrix} \begin{pmatrix} x_{s_1} \\ x'_{s_1} \\ \xi \end{pmatrix}, \tag{2.20}$$

with $m_{23} = dD_x/ds(s_2)$ and a new, more accurate transport matrix of the accelerator can be again calculated from the elementary matrices.

The momentum spread in the beam is also a source of the betatron tune (Q) spread, called chromaticity: $\frac{\mathrm{d}Q}{\mathrm{d}\xi}$, $\xi = \frac{\Delta p}{p}$. It comes from the $Br = \frac{p}{e}$ term in the denominator of the focusing strength of a quadrupole equation:

$$k = \frac{1}{Br}\frac{\mathrm{d}B_y}{\mathrm{d}x}. \tag{2.21}$$

Particles with lower momentum are deflected more than those with nominal momentum. Momentum spread causes a spread in the focusing strength of the quadrupole magnets:

$$\frac{\Delta k}{k} = \mp \frac{\Delta p}{p}. \tag{2.22}$$

It is possible to correct the chromaticity by installing sextupole magnets close to the quadrupoles, as shown in Figure 2.4. The focusing strength of these magnets grows linearly with the distance from their central axis, in one plane. The linear dependence of the displacement of the particle paths on their momentum spread Δp makes chromaticity correction possible. To correct the chromaticity in both horizontal and vertical planes, at least two sextupole families are necessary.

Chromaticity and large momentum spread make the particle transport non-linear. The coefficients of the transport matrix in Equation 2.20 become functions of the particle momentum deviation, the divergence and the transverse position.

2.2 TOTEM Experiment

The purpose of TOTEM experiment [6, 7, 8] is the measurement of the total proton-proton cross-section with the luminosity-independent method based on the Optical Theorem [9]. To achieve that, a detailed analysis of the elastic scattering cross-section at four-momentum[3] transfer squared of as little as $|t| \sim 10^{-3}\text{GeV}^2$ as well as the measurement of the total inelastic rate are necessary. Additionally, the physics programme of TOTEM includes studying the structure of a proton in elastic scattering with large momentum transfers and via diffractive processes, partially in cooperation with CMS [10], which is located at the same interaction point (IP5). As a result, the scope of physics in TOTEM's programme is complementary to CMS, which meant its detectors had to be designed with the capability of triggering and recording events in the very forward region.

Good acceptance for particles moving at very small angles with respect to the beam is required to perform these measurements. The two telescopes for inelastically produced particles (Figure 2.7) on both sides of the interaction point provide TOTEM with coverage in the pseudorapidity[4] range

[3]Energy and vector momenta of a particle can be combined into a four(dimensional)-vector $p = [E, -p_x, -p_y, -p_z]$.

[4]The rapidity y is defined as $y = \frac{1}{2}\ln\left(\frac{E+p_z}{E-p_z}\right)$, where E is the total energy and p_z is the longitudinal momentum component. The pseudorapidity η is defined as $\eta = -\ln(\tan(\frac{\Theta}{2}))$,

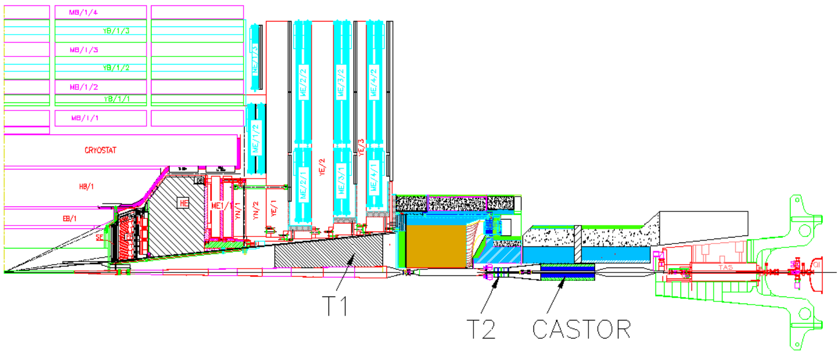

Figure 2.7: TOTEM forward detectors: T1 and T2 located near the CMS detector. The planned forward calorimeter CASTOR is also visible.

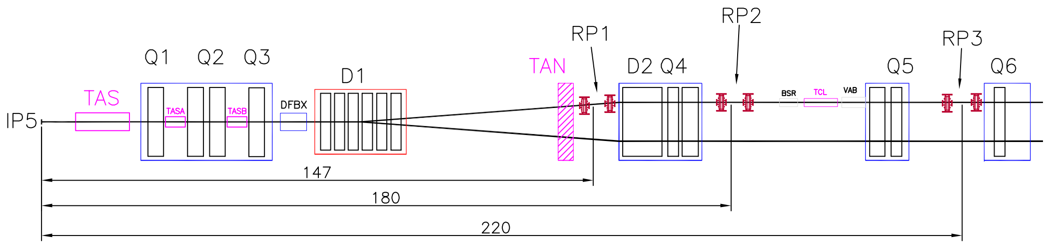

Figure 2.8: Location of the Roman Pot detectors at 147 m (RP1), 180 m (RP2, planned) and 220 m (RP3).

of $3.1 \leq |\eta| \leq 6.5$. Further coverage is provided by detectors placed in special movable beam-pipe insertions (called Roman Pots) installed at 147 and 220 m from the interaction point, designed to track leading protons at a few mm from the beam centre (Figure 2.8).

T1 telescope, the detector closest (9m) to the interaction point makes use of Cathode Strip Chambers (CSCs) [9], while T2 (installed at 13.5m) employs Gas Electron Multiplier (GEM) [11] detectors. The proton detectors in the Roman Pots (Section 2.2.4) are silicon devices custom-designed in order to meet TOTEM requirements, with the insensitive area at the edge facing the beam reduced to only 50 microns. This efficiency starting right at the physical detector edge is essential to maximising the experiment's acceptance of elastically or diffractively scattered protons at microradian angles. Additionally, special beam optics were designed to further optimise the acceptance and the resolution of proton detection (Section 2.2.2).

where Θ is the angle between the particle and the undeflected beam. For particles whose momentum $p \gg m$, rapidity and pseudorapidity are approximately equal.

Data read-out from all TOTEM detectors is handled by custom-developed digital VFAT chips [12], while the TOTEM Data Acquisition System (DAQ) is designed to be compatible with the CMS DAQ, enabling combined data taking.

2.2.1 Physics programme

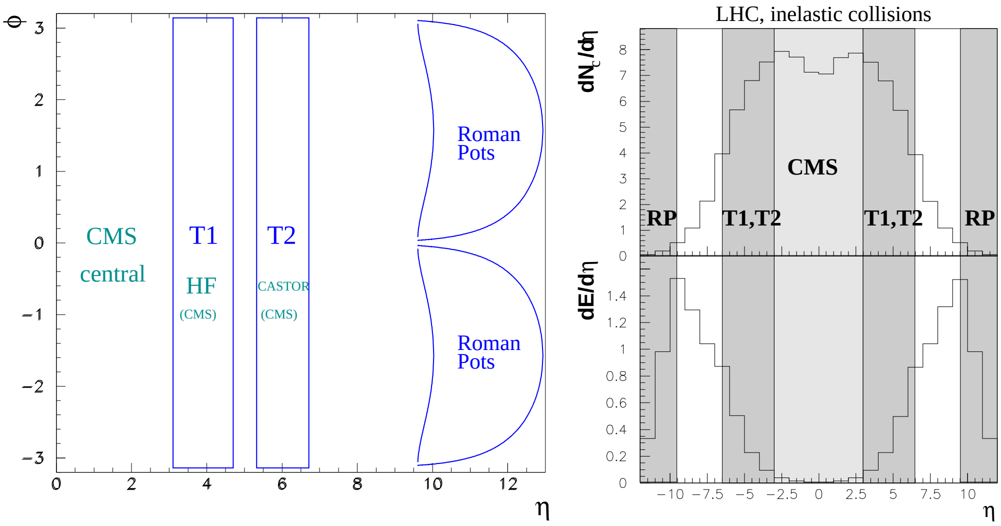

Figure 2.9: Left: Detector coverage in the pseudorapidity-azimuth plane by TOTEM and CMS detectors. Right: pseudorapidity distribution of charged particle multiplicity and energy flow for generic inelastic collisions at 14 TeV.

The exceptional coverage of high rapidities (Figure 2.9, left) makes the TOTEM's set of detectors well-suited for the study of elastic and diffractive proton scattering and other forward phenomena. Due to peaks in the forward regions of energy flow and charged particle multiplicity of generic inelastic events (Figure 2.9, right), TOTEM is able to accept up to 99.5% of all non-diffractive minimum bias events.

The key application of this high acceptance at high rapidities is the luminosity-independent measurement of the total cross-section based on the Optical Theorem.

Elastic proton scattering

Studying elastic scattering and soft inelastic diffraction is one of the main areas of interest for TOTEM. High-energy elastic nucleon scattering represents a collision process in which the most precise data over a wide energy range have been gathered [13]. The differential cross-section of elastic pp interactions at the LHC, as predicted by different models [14], is given in Figure 2.10. Due to large differences between the models in the highest en-

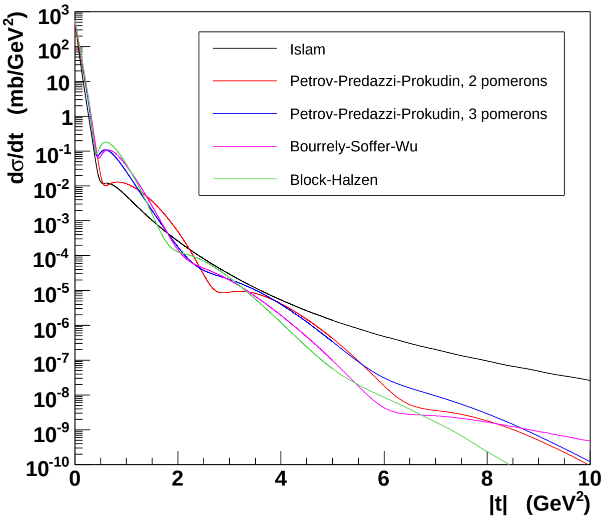

Figure 2.10: Differential cross-section of elastic scattering at 14 TeV as predicted by various models.

ergy region, a high-precision measurement up to $|t| \cong 10\text{GeV}^2$ will validate these models and help us understand the internal structure of the proton. Such high $|t|$ allows looking deeper inside the proton with high resolution.

For a moment, let us treat the pp collision as if the proton was placed in a microscope and probed with another proton beam. Assuming the beam itself consists of point-like particles, the resolution is limited by the de Broglie wavelength of these particles, which is $\lambda = \frac{h}{p}$, where p is the beam momentum and h is Planck's constant. Beams of high momentum therefore have small wavelengths and high resolution. By analogy to the optical microscope, the resolution becomes: $\Delta r \simeq \frac{\lambda}{sin\Theta} = \frac{h}{(psin\Theta)} \simeq \frac{h}{sqrt(|t|)}$, where Δr is the spatial resolution, Θ is the scattering angle and t is the four-momentum transfer squared [15].

The elastic scattering differential cross-section extends over 11 orders of magnitude and has therefore to be measured with several different optics scenarios. With different beam optics and running conditions (Section 2.2.2), TOTEM will cover the $|t|$-range from $2 \times 10^{-3}\text{GeV}^2$ to about 10GeV^2 (see also Figure 6.1, left).

Diffractive proton scattering

A broad class of processes at high energies has properties analogous to the classical diffraction of light that occurs when a beam of light meets an obstacle whose dimensions are comparable to its wavelength. These, by analogy, are usually called diffractive processes.

Diffractive scattering, consisting of Single Diffraction, Double Diffraction, Central Diffraction (Double Pomeron Exchange) and higher order (Multi Pomeron) processes, represents about 15% of the total cross-section in 14TeV centre-of-mass collisions. Many details of these processes related to the internal proton structure and low-energy QCD are still a mystery. The majority of the diffractive events (Figure 2.11) results in intact (leading) protons in the final state, described by their four-momentum transfer squared t and fractional momentum loss $\xi = \frac{\Delta p}{p}$. Such protons, when detected by Roman Pot detectors located at a distance from the interaction point, will be evidence that one of these events has occured. The other signature of diffractive events - large gaps in the event products' rapidity distribution due to exchange of colour singlets (Pomerons) between the interacting protons - will be detectable when the CMS and TOTEM detectors run in common data taking mode, as discussed in [10]. However, even stand-alone, TOTEM will be able to measure $\xi-$, $t-$ and mass distributions in soft Double Pomeron and Single Diffraction events.

2.2.2 LHC running scenarios for TOTEM

As discussed in section 2.1.2, the properties of the optics can be expressed by the two optical functions L (effective length) and v (magnification), which are defined by components a and b of the matrix M in Equation 2.14, respectively (a more detailed discussion can be found in [16, 17]).

The transverse displacement $(x(s), y(s))$ of a proton at a distance s from the interaction point (IP)[5] is related to its original displacement (x^*, y^*) and its momentum vector (expressed by the horizontal and vertical scattering angles Θ^*_x and Θ^*_y and by $\xi = \frac{\Delta p}{p}$) at the IP via the optical functions and the horizontal dispersion $D_x(s)$ of the accelerator:

$$\begin{aligned} y(s) &= v_y(s) \cdot y^* + L_y(s) \cdot \Theta^*_y \\ x(s) &= v_x(s) \cdot x^* + L_x(s) \cdot \Theta^*_x + \xi \cdot D_x(s) \end{aligned} \tag{2.23}$$

For the total cross-section measurement with luminosity-independent method TOTEM has to reach the lowest possible values of the squared four-momentum

[5] The "*" superscript of the optical parameter denotes its value in the interaction point.

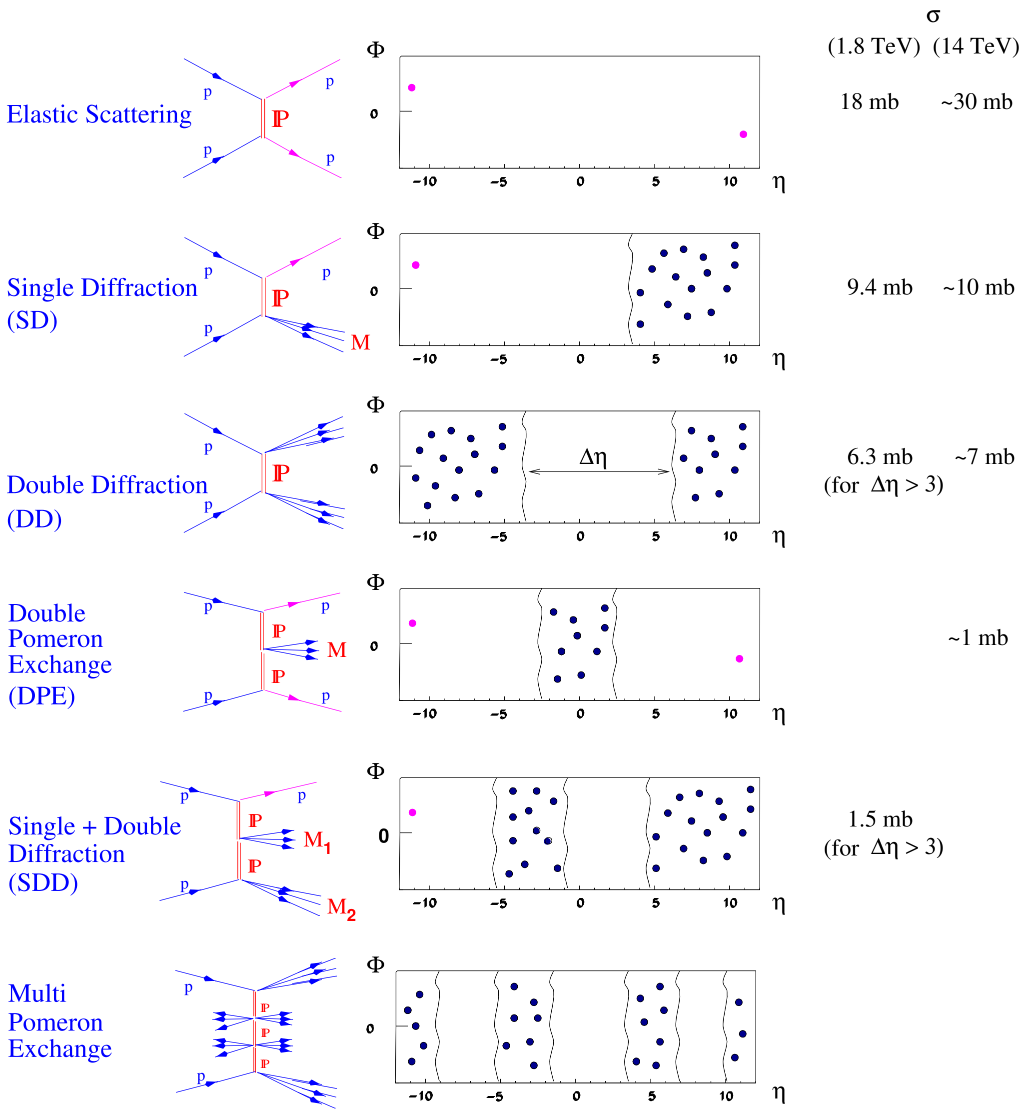

Figure 2.11: Different classes of diffractive processes classes and their cross-sections as measured at Tevatron and estimated for the LHC.

transfer $-t \sim p^2\Theta^2$ in elastic pp scattering. Scattered particles travelling close to the beam can be detected on both sides of the IP provided the displacement at the detector location is large enough (at least $10\sigma_{beam}$ from the beam centre) and if the beam divergence at the IP (proportional to $\frac{1}{\sqrt{\beta^*}}$, see Equation 2.10), is small compared to the scattering angle. Such conditions require special high-beta optics: the larger the β^*, the smaller the beam divergence is.

Two special sets of LHC optical parameters (optics) are foreseen for

TOTEM: one with $\beta^* = 1535\,\mathrm{m}$, expected to be viable at a later stage of operation and one with $\beta^* = 90\,\mathrm{m}$. The latter uses standard injection optics and typical early LHC running beam conditions: zero degree crossing-angle and up to 156 bunches with low luminosity.

The different running scenarios dictated by TOTEM's physics programme have to be adjusted to the LHC commissioning in the first years of operation. TOTEM will thus attempt to take data even in unoptimal optics conditions, adapting the trigger patterns to current luminosity, which should be possible with the DAQ allowing trigger rates up to a few kHz without involving a higher level trigger.

As mentioned before (Equation 2.23), the beam divergence is a limiting factor of the $\Theta^*_{x,y}$-reconstruction resolution and thus the resolution of t. Table 2.2 shows a summary of the optical function and beam parameters as well as Roman Pot distances from the beam for different running scenarios.

β^* [m]	L_x [m]	L_y [m]	v_x	v_y	D_x [m]	x_{RP} [mm]	y_{RP} [mm]	$\sigma(x^*)$ [μm]	$\sigma(\Theta^*_x)$ [μrad]
0.5	1.5	18	-3.9	-3.8	-0.080	1.26	6.0	16.6	30
2	0.49	18	-3.5	-4.0	-0.086	1.6	3.7	32	16
90	0	262	-1.9	0.0	-0.041	4.5	6.8	212	2.3
1535	100	270	0	0	-0.05	0.8	1.3	450	0.3

Table 2.2: Optics parameters at IP5 and at the RP220 station for the TOTEM running scenarios. L_x, L_y, v_x, v_y and D_x are the parameters of the Equation 2.23 at RP220, x_{RP} and y_{RP} are the distances of the horizontal and the vertical Roman Pots of the RP220 station from the beam centre, respectively, $\sigma(x^*)$ is the beam size and $\sigma(\Theta^*_x)$ is the beam divergence at IP5.

β^* [m]	k	$N/10^{11}$	$\mathcal{L}$ [$\mathrm{cm}^{-2}\mathrm{s}^{-1}$]	$\lvert t\rvert$-range for $\xi = 0$ [GeV^2]	$\lvert\xi\rvert$-range
1535	43 – 156	0.6 – 1.15	$10^{28} - 2\cdot 10^{29}$	0.002 – 1.5	< 0.25
90	156	1.15	$3\cdot 10^{30}$	0.02 – 10+	< 0.25
11	936 – 2808	1.15	$3\cdot 10^{32}$	0.6 – 8	0.02 – 0.2
0.5 – 2	936 – 2808	1.15	10^{33}	1 – 10+	0.02 – 0.2

Table 2.3: Running scenarios for different β^* values. k is the number of bunches and N is the number of protons per bunch.

The high-β^* runs (Table 2.3) with 156 bunches, zero degree crossing-angle and maximum luminosity between 10^{29} and $10^{30}\mathrm{cm}^{-2}\mathrm{s}^{-1}$, will concentrate on low-$|t|$ elastic scattering, total cross-section, minimum bias physics and soft diffraction. A large fraction of forward protons will be detected even at the lowest $|\xi|$ values. Low-β^* runs with more bunches and higher luminosity (10^{32} - $10^{33}\mathrm{cm}^{-2}\mathrm{s}^{-1}$) will be used for large-$|t|$ elastic scattering and diffractive studies for $-\xi > 0.02$.

2.2.3 T1 and T2 detectors

Since the expected products of inelastic events cover a rapidity range of about 4 units, TOTEM's forward telescopes dedicated to the measurement of the inelastic rate have to be installed in the forward regions of CMS (Figure 2.7) on both sides (arms) of the IP in order to detect as many particles from such events as possible.

T1, covering pseudorapidity range of $3.1 \leq |\eta| \leq 4.7$ consists of two arms, with 5 planes per arm, each housing 6 trapezoidal Cathode Strip Chambers (CSC) are planned to be installed in the CMS End Caps between the vacuum chamber and the main magnet, at a distance of 7.5 to 10.5 m from the IP.

T2 covers pseudorapidity range between 5.3 and 6.5 and is made of 20 semi-circular sectors of Gas Electron Multiplier (GEM) detectors in each of two arms. It is installed between the vacuum chamber and the inner shielding of the CMS forward hadron calorimeter (HF) at 13.5 m from the IP.

Both of these detectors provide a fully inclusive trigger for minimum bias and diffractive events, with an expected loss of a few per cent of the inelastic event rate. Owing to their location, they allow the reconstruction of the primary vertex of an event to distinguish real beam-beam collision events from the background (for example, beam scraping by the collimators). Additionally, their symmetrical location with respect to the IP enables better control over systematic uncertainties in event reconstruction calculations.

In addition to the measurement of the total inelastic rate, T1 and T2 will be the key detectors for the study of inelastic processes either by TOTEM or by the joint CMS/TOTEM experiments [10]. At low luminosities ($L < 10^{31}\mathrm{cm}^{-2}\mathrm{s}^{-1}$), they can measure the integrated inclusive Single Diffractive (SD) and Double Pomeron Exchange (DPE) cross-sections, as well as their dependence on four-momentum transfer t and mass of the diffractive system M. Such events have unambiguous signatures in TOTEM and can be easily triggered by requiring at least one track in T1/T2 when the proton(s) are detected in the Roman Pots.

At higher luminosities, between 10^{31} and $10^{33}\mathrm{cm}^{-2}\mathrm{s}^{-1}$, T2 can be used in the joint CMS/TOTEM experiment for hard diffraction and forward physics studies. The ability to use T2 track information may also be of use in studying rare physics processes such as single-diffractive proton dissociation into three very forward jets.

2.2.4 Roman Pot detectors

Roman Pot is the usual name for movable box-shaped particle detector devices which can be inserted into the vacuum pipe (in which the beam circulates) of an accelerator (see Figure 2.12). The detectors themselves are

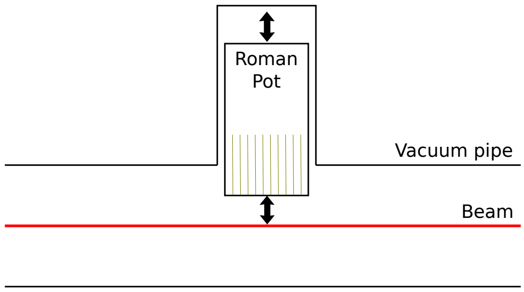

Figure 2.12: A schematic view of a Roman Pot device insertion into a beam pipe.

put in a vacuum container called a "pot" which separates them from the vacuum of the accelerator pipe (usually via a thin window) to prevent stray particles of the detector materials from leaking into the primary vacuum. Such detectors were invented for the purpose of detecting particles at very small angles from the beam (on the order of *mrad*).

The application of such devices for detection of leading protons was first done at the ISR[6] between 1971 and 1972. Afterwards, their use was adopted in successive accelerators, such as SPS, Tevatron, RHIC and DESY.

Due to unique operating conditions of the LHC machine, the Roman Pot detector devices of the TOTEM experiment had to be designed taking into account the microscopic cross-section and the high luminosity of the beam, the accompanying high irradiation and the ultra-high vacuum in the pipe.

TOTEM Roman Pots design

The Roman Pot detector devices of the TOTEM experiment contain 10 planar microstrip detectors per pot. Five of the planes have their strips aligned at 45° with respect to the active edge of the detector, while the other five are aligned perpendicularly (see Figure 2.13). The detectors are placed so that the strip directions alternate between consecutive planes. Being able

[6] Intersecting Storage Rings, the world's first hadron collider at CERN

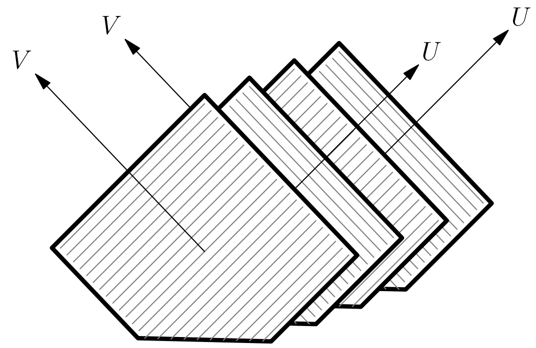

Figure 2.13: A schematic view of sensitive strips on Roman Pot silicon detectors.

to take readings from five planes makes it easier to distinguish real tracks in an event from unrelated background events.

The advantage of this alignment is that the particle hit profiles are equivalent in both directions. The disadvantage, however is that with only two directions it is difficult to reconstruct particle tracks in high multiplicity events.

Due to the small cross-section of the beam, the detectors need to be placed extremely close to the beam in order to achieve high acceptance. The parameters of the LHC beam enforced the development of new technologies for the Roman Pots. The end result are radiation-resistant detectors whose active edge facing the beam has a dead area of only $\sim 50\,\mu m$ and their distance from the thin window (only $150\,\mu m$ thick) at the bottom of the pot is $200\,\mu m$. The pots are positioned at 10ρ from the beam centre.

Each pot is a box measuring 54 by 128 by 135 mm made of stainless steel (see Figure 2.14). There are six such pots in each station and 24 in total (in four stations[7]).

Precision positioning of the pots with respect to the beam pipe is ensured by the use of micro-stepping motors, which can move the insertions with $5\,\mu m$ theoretical precision. The real precision, however, depends on the quality of assembly. Relative position from the nominal beam centre is provided by angular resolvers embedded in the stepper motors, while absolute position is provided by additional LVDT[8] sensors.

[7]A Roman Pot station consists of two groups of three pots, two of which are placed vertically (top and bottom pots) and one horizontally.

[8]Linear Variable Differential Transformer is a type of transformer used for measuring displacement. It consists of three coils in a tube through which a ferromagnetic core

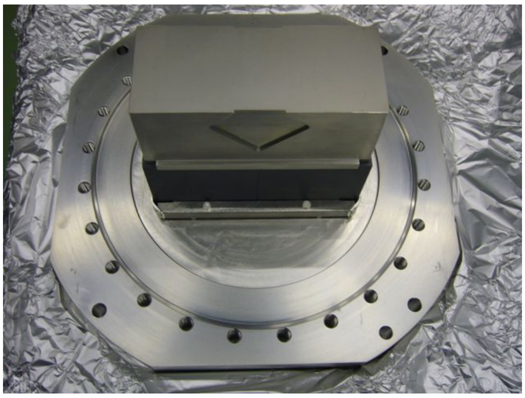

Figure 2.14: A picture of a complete Roman Pot box. The black ferrite collar is needed to reduce the beam coupling impedance.

Silicon detectors

Due to their suitability [18] for precise tracking of charged particles travelling at very low angles to the beam, silicon-based sensors were used in TOTEM's Roman Pot detectors. The use of microstrip detectors allows achieving hit position reconstruction resolution of less than $20\,\mu m$. However, the precise value depends on the spacing (pitch) of sensitive elements.

The basic principle is to create doped regions on the surface of the silicon and apply reverse voltage to the resulting diodes. When a charged particle passes through semiconducting material, it interacts with its electrons, transferring energy. As a result, the electrons move into the conduction band and become free charge carriers. This causes small ionisation currents, which can be measured precisely.

Microstrip detectors (Figure 2.15) consist of p-n junctions arranged into parallel strips. The junctions are formed between thin, highly p-doped strips and lightly n-doped body with a thin, highly n-doped layer beneath.

Signal from a strip is generated from collected charge carriers after a charged particle creates a "track" of electron-hole pairs in its wake as it passes through the bulk of the detector and passed to a read-out channel connected to the strip. The application of reverse biasing voltage creates an electric field in the entire n region, which allows all generated free charge carriers to be collected after particle hit.

Biasing voltage also decreases the charge collection time and reduces the effects of charge sharing (in case a particle passes through the detector at an angle) and charge diffusion due to thermal excitation. The biasing of the

attached to the measured object is driven.

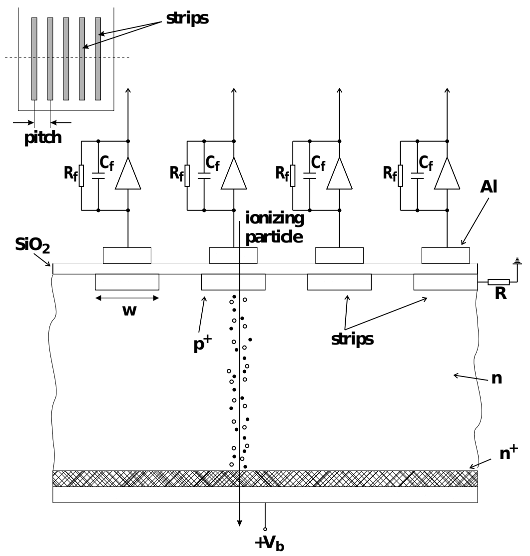

Figure 2.15: Top view and a cross-section (along the dashed line) of a microstrip detector. The strips are AC-coupled to the readout electronics by a thin insulating silicon dioxide layer between the strip and the aluminum layer.

strips is discussed in detail in [18].

The actual signal from the detector is too weak for direct measurement and must be amplified with a preamplifier, which is mounted as close as possible to the detector to minimise losses on the connecting wires. Charge-sensitive preamplifier was selected due to its insensitivity to thermal variations of intrinsic detector capacitance. The preamplifier works by integrating the incoming charge on its capacitor. The output voltage is then proportional [19, 20] to the charge:

$$V_{out} \simeq -\frac{Q_{in}}{C_f},$$

and the output signal does not depend on the input capacitance. The collected charge must be discharged before the next measurement. This is done by adding a feedback resistor in parallel, which discharges the capacitor with a time constant $\tau_{reset} = C_f R_f$.

Each detector channel has an associated value of equivalent noise charge, which describes the amount of noise in terms of a charge pulse at the detector needed to produce the same output. [21] contains detailed description of the types of noise in a silicon detector and their sources.

The microstrip detectors in TOTEM's Roman Pots are AC-coupled. The coupling is done by a capacitor created by a thin layer of silicon dioxide placed between the p-doped strip and the metal contact of the read-out electronics.

Silicon detectors are typically produced with standard planar technology, which requires multi-ring terminating structures at the cut edges Voltage Terminating Structure (VTS). A set of rings suitable for high-radiation environment introduces a dead area of around 1 mm, which makes such detectors unusable in the operating conditions of the TOTEM experiment, where full sensitivity as close to the edge facing the beam as possible is required. To alleviate this issue, detectors with Current Terminating Structure (CTS). For such detectors, the charge collection efficiency increases quickly within tens of micrometres from the cut edge [22, 23].

Chapter 3

Monte Carlo simulations of particle interactions

3.1 Interactions of particles with matter

A particle passing through matter interacts with its atoms (both nuclei and their electrons). Electromagnetic interactions are the main contribution to the particle's energy loss, freeing electrons from the material's atoms in the process. Detecting such free charge carriers by applying a reverse polarity voltage to electrodes connected to a semiconductor is the basic function of semiconductor detectors. In high energy physics, the main application of such devices is particle tracking.

The stopping power, defined as $S = -\frac{dE}{dx}$, represents the amount dE of energy lost by a charged particle in matter over a travelled distance dx and is expressed by the Bethe-Bloch formula [24, 25, 26]:

$$-\frac{dE}{dx} = kz^2\frac{Z}{A}\frac{1}{\beta^2}[\frac{1}{2}ln\frac{2m_ec^2\beta^2\gamma^2T_{max}}{I^2} - \beta^2 - \frac{\delta}{2}], \tag{3.1}$$

with parameters given in Table 3.1:

The density effect, which becomes significant for relativistic particles is included in the δ parameter. The maximum kinetic energy which can be transfered between the particle and a free electron in a collision to a free electron in a single collision T_{max} is given by [26]:

$$T_{max} = \frac{2m_ec^2\beta^2\gamma^2}{1 + \frac{2\gamma m_e}{M} + (\frac{m_e}{M})^2},$$

where m_e is the mass of the electron and M is the mass of the incident particle.

Parameter	Description
$k = 4\pi N_A r_e^2 m_e c^2$	$= 0.31\,\text{MeV}\cdot\text{g}^{-1}\text{cm}^{-2}$
z	atomic number of the incident particle
Z	atomic number of the lattice atoms
A	atomic mass of the medium
T_{max}	maximum kinetic energy transferred to a free electron in an interaction
I[eV]=$(10 \pm 1) \cdot Z$	mean ionisation potential per atomic electron
δ	density effect correction to ionisation energy loss

Table 3.1: Parameters related to Equation 3.1.

For high-energy particles the maximum transferable energy T_{max} is almost equal to their total energy, but the probability of such transfer is very low. The energy loss in transfers below a certain value (T_{cut}) is approximately equal to the energy deposited in a thin detector [19]. For simplicity, a modified stopping power formula, called "restricted energy loss", which excludes energy transfers over T_{cut} is often used instead [27]. Obviously, the energy loss of the particle itself is not restricted, just its result in a detector. The stopping power S in silicon as a function of the incident particle energy is shown in Figure 3.1. The stopping power becomes constant and independent of the thickness if the detector is thin and if the passing particles are relativistic ($\beta\gamma \geq 3$). Such particles passing a thin detector are called minimum ionising particles (MIP).

In case of 7 TeV protons passing through silicon detector, the mean energy loss is 99 keV for a thickness of $300\,\mu m$, which is negligible compared to the original energy. This lets us consider the silicon detectors used in the Roman Pots as thin. The energy loss given by the Bethe-Bloch formula is statistically distributed around its mean value due to the random nature of the energy loss process. The distribution, often referred to as "energy straggling", is approximately Gaussian for thick absorbers, but develops asymmetry and a tail towards high energies for decreasing thickness; it becomes a Landau distribution [28] for very thin absorbers.

3.2 Geant4 Monte Carlo simulation software

Physics experiments require modelling and simulation of the theoretical processes in order for the scientists to be able to understand what is really

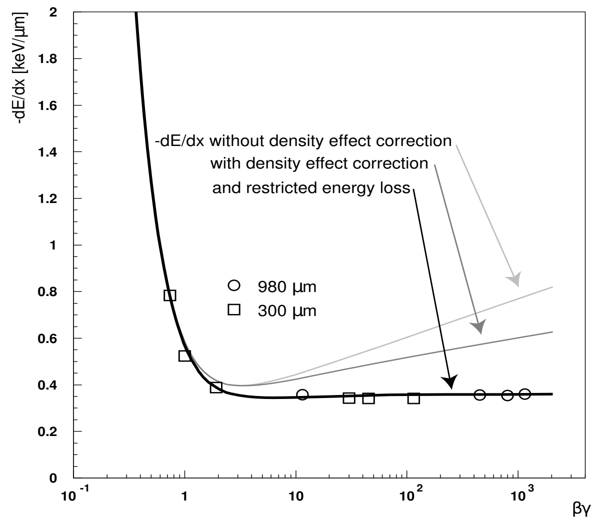

Figure 3.1: Mean energy loss in silicon as a function of reduced incident particle momentum ($\frac{p}{mc} = \beta\gamma$). The density effect and the restriction of the maximal energy loss T_{max} to T_{cut}=500 keV become important at high energies. The circular (rectangular) data were gathered with a 980 μm (300 μm) thick detector [19].

happening and how to analyse the results. Complicated, large scale experiments such as LHC need powerful tools to model the experimental machines, the detectors and the investigated objects - particles in this case. This means modelling and simulating the passage of particles through matter, by means of Monte Carlo simulation software. One of the toolkits providing the means to perform Monte Carlo simulations is Geant4 [35].

The toolkit provides the ability to create a geometrical model of an experimental apparatus with a large number of components of different shapes and materials, and to define "sensitive" elements that record information (hits) needed to simulate detector responses (digitisation). The primary particles of an event can be derived from internal and external sources. Geant4 contains a very complete set of physics processes to model the behaviour of particles. It is possible to choose from different approaches and implementations, and to modify or add to the set provided. Physics process models include electromagnetic, hadronic and optical processes, known and theoretical particle properties over a wide range of energies.

The simulation of the passage of particles through matter can be divided into:

- geometry and materials

- particle interaction in matter
- tracking management
- digitisation and hit management
- event and track management

3.2.1 Detector geometry and materials description

The geometry module offers the ability to describe a geometrical structure and propagate particles through it. The description conforms to the ISO STEP standard, enabling the exchange of detector geometry data with CAD systems.

In Geant4 the shape of a logical volume can be defined by means of solids. Solids with simple shapes, like rectilinear boxes, trapezoids, spherical and cylindrical sections or shells, each have their properties coded separately, according to the concept of Constructive Solid Geometry (CSG). More complex solids are defined by their bounding surfaces, which can be planes, second order surfaces or higher order B-spline surfaces, and belong to the Boundary Representations (BREPs) sub-category. This variety matches those described by the ISO STEP standard for CAD systems. Another way of obtaining solids is by boolean combination – union, intersection and subtraction. The solids should be either CSGs or other boolean solids (the product of a previous boolean operation). One of the components may have an optional transformation relative to the other.

A logical volume represents a detector element of a certain shape that can contain other volumes inside it and have other attributes; it also has access to other information that is independent of its physical position in the detector, such as material and sensitive detector behaviour. A physical volume represents the spatial positioning of the logical volume with respect to an enclosing parent (logical) volume. Thus a hierarchical tree structure of volumes can be built, each volume containing smaller volumes (which may not overlap). Repetitive structures can be represented by specialised physical volumes — copies and parameterised placements – sometimes with significant savings of memory. All physical volumes are assigned a material corresponding to the modelled object. Materials are defined by their isotope or element composition and density. Elements can be specified by the average atomic weight or as a mixture of their isotopes.

Although a detector is naturally and best described by a hierarchy of volumes, efficiency is not critically dependent on this. An optimisation technique, called voxelisation, described in [35] allows efficient navigation even in "flat" geometries, typical of those produced by CAD systems.

3.2.2 Physics processes modelling

The Geant4 toolkit contains a large variety of complementary and sometimes alternative physics models covering the physics of photons, electrons, muons, hadrons and ions from 250 eV up to several PeV.

For a particle interaction or decay it is useful to distinguish between the process, i.e., a particular initial and final state, which therefore has a well-defined cross-section or mean life, and the model that implements the production of secondary particles. This allows offering multiple models for the same process.

A particle in flight is subject to many competing processes. Moreover, in a real detector, it will often travel through many regions of different materials, shapes and sizes before interacting or decaying.

Processes other than interaction or decay also compete to limit the step. Continuous energy loss may limit the step to preserve precision. Also, transportation insists that the step should not cross a geometrical boundary. A maximum allowed step can also be set manually.

The process which returns the smallest distance is selected and its post step action is invoked. If it is an interaction or decay, the particle is destroyed and secondary particles are generated. If not, the particle gets another chance to interact or decay.

3.2.3 Tracking

The overall performance of detector simulation depends mostly on the CPU time spent moving each particle by one step. As a consequence of this, the particles in Geant4 are transported, instead of self moving. This is done by the transportation process. The tracking category simply controls the invocation of processes.

Physics processes are treated in a very generic way. Tracking does not depend on the particle type or on the specific physics process, including particle transportation. Each particle is moved step by step with a tolerance that permits significant optimisation of execution performance but still preserves the necessary tracking precision. All physics processes associated with the particle propose a step. For a particle at rest this is time rather than length. Depending on its nature, a physics process possesses one or more characteristics represented by the following actions handled by the tracking:

- at rest, for particles at rest (e.g., decay at rest);
- along step, which implements behaviour such as energy loss or secondary particle production that happen "continuously" along a step (e.g. Cherenkov radiation);
- post step, which is invoked at the end of the step (e.g. secondary particle production by a decay or interaction).

Along step actions take place cumulatively, while the others are exclusive. The tracking handles each type of action in turn. A process can indicate that its action must always be executed (multiple scattering and transportation are examples). The tracking scans all physics processes and actions for the given particle, and decides which one is to be invoked.

3.2.4 Hits and digitisation

In Geant4, a hit is a snapshot of a physical interaction or an accumulation of interactions of a track or tracks in a "sensitive" detector component. The term digit represents a detector output, for example, an ADC/TDC count or a trigger signal. A digit is created from one or more hits and/or other digits. Given the wide variety of applications of Geant4, the ways of describing detector sensitivity and the quantities that need to be stored in the hit and/or digit vary greatly.

A sensitive detector creates hits using the information given in the current step. For each detector type, a custom implementation of the detector response must be provided. Hits are collected in an event object. At tracking time, when the step is inside of a volume which has a pointer to a sensitive detector, this sensitive detector is invoked with the current step information.

In contrast to sensitive detector, which is invoked automatically at tracking time, the digitisation module must be invoked by the user's code. Digitisation may be done during event processing, at the end of each event, and/or even after some number of events had been processed to simulate "pile-up".

The readout segmentation can be different to the geometrical structures of the detector in some cases. For example, the user may implement a detailed sandwich structure of a sampling calorimeter, while the readout collects the energy deposition of some of the layers. The readout geometry is an artificial geometry which can be associated with a sensitive detector. Each sensitive detector can have its own readout geometry. (Note that the transportation process does not see the volume boundary of readout geometry and thus a step does not end at the boundary of readout geometry.) Once a step belongs to a sensitive detector, geometrical information of both the "real" tracking and the readout geometry geometries are available to the sensitive detector.

Chapter 4

TOTEM offline software

4.1 Simulation software

To analyse proton acceptance and reconstruction resolution for different LHC running scenarios in detail, the TOTEM experment designed and developed a software model of the Roman Pot detectors. Due to overlapping physics programmes and common data taking infrastructure with CMS, the CMS software framework (CMSSW)[29] and storage model[30] were used as basis for the TOTEM software. Owing to CMSSW's modular structure, TOTEM software could be easily added on top of it.

The Roman Pot simulation software, discussed in detail in the following sections, can calculate the digital response of all Roman Pot detectors to the forward protons originating from an event at the interaction point 5.

A schematic overview of the software with its main components is shown in Figure 4.1. All components can be configured according to a specific running scenario.

The Roman Pot stations and the adjacent beam pipes are described using DDL[31] in the geometry data files. The software enables the simulation using both ideal and displaced detector packages.

The simulation begins with an external Monte Carlo event generator [32], such as Phojet [33] or Pythia [34], although any generator for which a suitable interface exists can be used.

MC generators in general produce events with the assumptions of parallel trajectories of incident particles and ideal collision vertex position. In reality, the proton parameters vary according to a certain distribution, which depends on the optics of a specific running scenario (see 2.1.2). Therefore, the position, the momenta, and the total energy of the event need to be modified (smeared) taking into account the beam size, divergence, energy spread

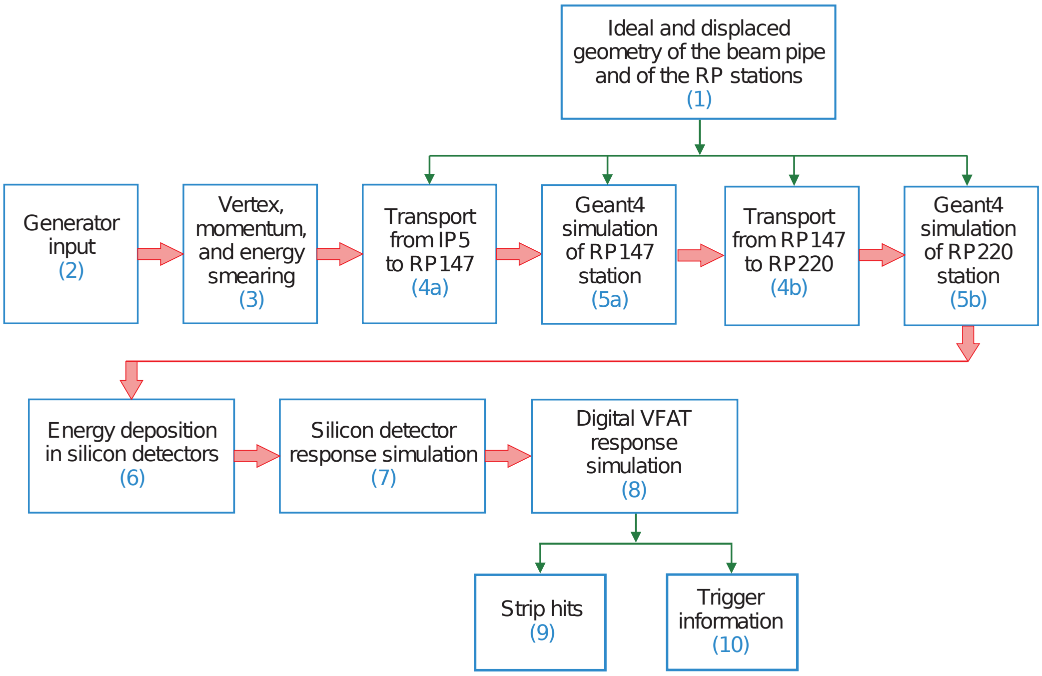

Figure 4.1: Work flow diagram of the Roman Pot simulation software. Red arrows show the order in which the modules are executed. Green arrows indicate the most important data inputs and outputs.

and the crossing angle.

Since the are two RP stations (at 147 and 220 m) on each side of IP5, some protons flying through the 147 m stations interact with the material of the detectors, which affects the trajectories of protons reaching the 220 m stations. As shown in [17], this effect is detectable and must be simulated accordingly, by processing the events in consecutive stations in sequence.

Simulation of the transport of forward protons through the accelerator lattice is done using special polynomial parameterisations [17] due to insufficient speed of the MAD-X lattice transport simulation software. Geant4 toolkit [35, 36] is then used to simulate the passage of protons through the Roman Pot devices and the energy deposition in the silicon detectors.

The simulated energy deposition is then used to calculate the signal response of the silicon detectors and the digital response of the VFAT chips based on their software models. The key parameters of these models are tuned according to the measurements taken during beam tests [16]. Detector and VFAT responses translate into strip hits, which are used as input for the reconstruction part of the software. Trigger patterns are used in TOTEM trigger studies to optimise the trigger algorithm.

4.1.1 Event generator

Three MC event generators are used for event simulation: Particle gun, PYTHIA and PHOJET. The particle gun is a simple event generator that generates an event with a certain number of particles of specific types at certain region of momentum space. In TOTEM, it is used mainly for the simulation of elastic events. PYTHIA is a general-purpose generator for hadronic events in proton-proton, electron-positron and electron-proton colliders and is used to simulate single diffraction (SD) events in TOTEM software. PHOJET is a specialised generator for detailed modelling of minimum bias events with a realistic superposition of various types of diffractive and non-diffractive particle production processes. In TOTEM, it is used for the simulation of Double Pomeron Exchange (DPE) events.

4.1.2 Beam smearing

The particles generated by a MC event generator are placed in the centre of the IP5 volume. The parameters of the colliding beams, however, are defined by optics-dependent distributions. To account for that, the energy, the momentum and the position of the colliding protons have to be smeared according to those distributions before the detector response to the proton tracks can be simulated [37]. The smearing process is shown in Figure 4.2.

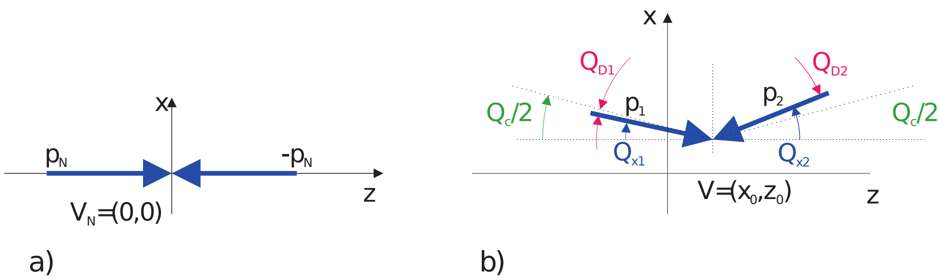

Figure 4.2: Left: Proton-proton collision from the Monte Carlo generator (X-Z projection used for clarity). The protons have nominal momenta $(\vec{p}_N, -\vec{p}_N)$ and the collision occurs at the (0,0) point. Right: The LHC proton-proton collision. The collision point is displaced. The protons collide at an angle which is the superposition of the IP5 crossing angle (Θ_C) and the beam divergence ($\Theta_{D1,2}$), which approximately follows a Gaussian distribution. The spread of the proton momenta ($p_{1,2}$) follows the beam momentum spread.

4.1.3 Proton transport

The motion of particles inside IP5 and inside the Roman Pot stations is performed by means of Geant4 simulation (described below), while their trajectory between these points (see Section 2.1.2) depends heavily on LHC optics and must be simulated with MAD-X, because this software was and is still used for LHC optics design and control. However, since MAD-X is too slow for direct usage in simulation and reconstruction, parametrised polynomial approximations [17] of the transport matrices for different running scenarios are used instead.

4.1.4 Geant4 simulation

Simulations of the detectors and the physical interactions of particles with them are performed with Geant4 QGSP physics list, which includes all required physics processes and particles for the simulations in at energies up to 10TeV. The possibility to use an user-defined parameterisation-based physics process, which is applied to certain particles in specified volumes offered by Geant4 was used for plugging in the fast simulation of the proton transport between IP5 and the Roman Pot detectors. The four Geant4 so-called "physics processes" are defined to perform the proton transport between the IP5 and the RP stations. Each of these processes is based on the proton transport parameterisation introduced in [17]. A parameterisation has to be calculated for each of the TOTEM running scenarios.

The layout of all TOTEM-related volumes used in Geant4 simulation is shown in Figure 4.3. MC-generated particles are injected near the centre of

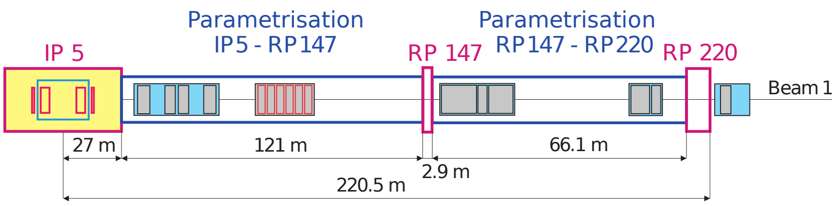

Figure 4.3: Geant4 simulation of the TOTEM detectors. The volumes of the IP5 hall and of the Roman Pot stations at 147 and 220 m (red rectangles) are fully simulated with Geant4 physics processes. Beam transport (blue rectangles) is performed with the optics-dependent parameterisation.

the interaction point. Subsequently, their passage is tracked through all detectors at IP5 (the main CMS detector and TOTEM's T1 and T2 telescopes) by Geant4. In the beam pipe outside the IP5 volume, the simulation is taken over by TOTEM's custom proton transport parametrisation, which carries the particles directly into Roman Pot station at 147 m. There, full Geant4 simulation is performed. Similarly, the surviving particles are transported into RP station at 220 m, where again, the simulation process is handed over to Geant4. As a result of the simulation, the energy deposits in the silicon detectors (and other detectors included in the simulation) are obtained for later usage in detector modelling and digitisation of the signal.

This approach has a significant advantage. The simulation is much simpler than full magnetic field simulation and much faster, while still retaining all the properties necessary for TOTEM acceptance and resolution studies, because the parametrisations are calculated to yield the same results as full MAD-X tracking (within TOTEM's maximum theoretical resolution) and the influence of the RP station at 147 m on the measurements at 220 m station is also taken into account.

The disadvantage, however, is that neither any interactions between protons and the elements of the LHC machine, nor any generated secondary particles from IP5 or RP147 station are simulated. For studying such phenomena, other software packages must be used [38, 39, 40, 41].

4.1.5 Detector response simulation

The energy depositions calculated by Geant4 are used to simulate the signal response of the silicon detectors. Energy deposition data contains information about the type of the particle that crossed a given detector, its entry and exit points, entry angle and energy loss. The simulation of the signal response shown schematically in Figure 4.4, takes into account all the above data, as well as the physical processes occuring (as discussed in in Section 3.1) when a charged particle traverses a thin silicon detector. Since Geant4 gives the amount of deposited energy in one step, the energy is first segmented depending on the angle of the incident particle and the required precision. Segments are then converted to charge clouds (with Gaussian distribution) and projected on the detector's surface. The charge induced in each strip is calculated, taking into account inter-strip coupling. Contributions from multiple tracks (if any) are added to each strip's response. Noise and non-functional strips can also be simulated. Finally, a map of charge collected by the VFAT input channels is produced.

4.1.6 VFAT chip response simulation

The real VFAT chip [16] has 128 input channels with comparators. For signal level higher than a certain (programmable) threshold received from a given channel, a logical 1 is produced in the output corresponding to that

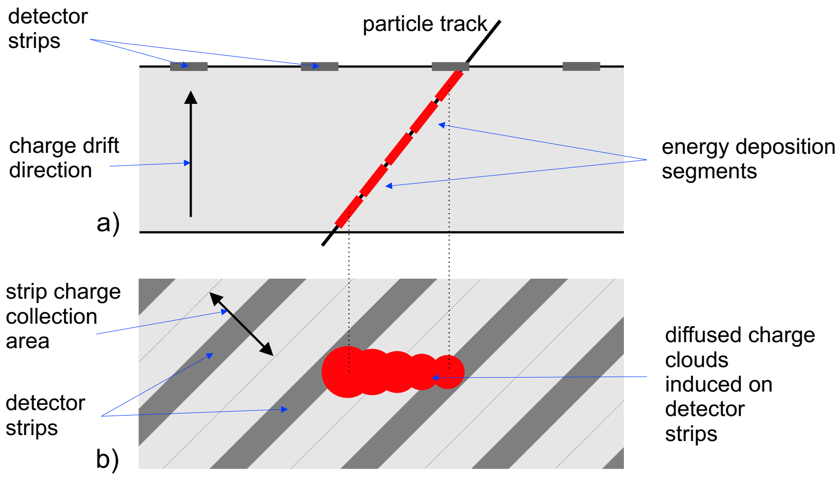

Figure 4.4: Simulation of the energy deposition in the silicon detector volume. (a) Cross-section view. (b) Top view.

channel. The digitisation simulates this function. The threshold value is expressed in elementary charges and is common for all channels. The resulting hits are stored in the Event for subsequent use by the reconstruction procedures. A typical hit profile of the RP220 vertical silicon detector can be seen in Figure 4.5.

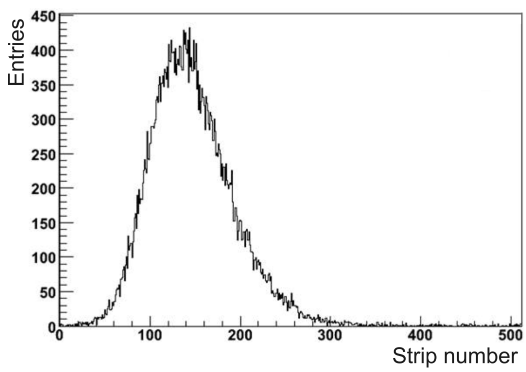

Figure 4.5: Hit profile of the RP220 vertical silicon detector, generated from a sample of elastically scattered protons, simulated with β^{*}=1535 m optics.

The VFAT chip can, apart from the hit information, also produce triggers. The input channels are grouped into sectors of 16-128 channels and the chip can provide information if any of the channels in a given group was hit very quickly. Between 1 and 8 can be selected for triggering. The produced triggers are recorded in the event data and can used in trigger analysis.

4.2 Reconstruction software

Some of the surviving protons from a collision event at the interaction point reach the Roman Pot stations and pass through the silicon detectors, depositing energy in their strips and producing hits. Based on the model of the LHC and these hits, the reconstruction packages of the TOTEM software can calculate the kinematic parameters of the protons emerging from the collision at the interaction point. Like the rest of the software, these packages are implemented in the CMSSW framework, described in detail in [29]. Figure 4.6 shows the main modules of this part of the software and their interactions.

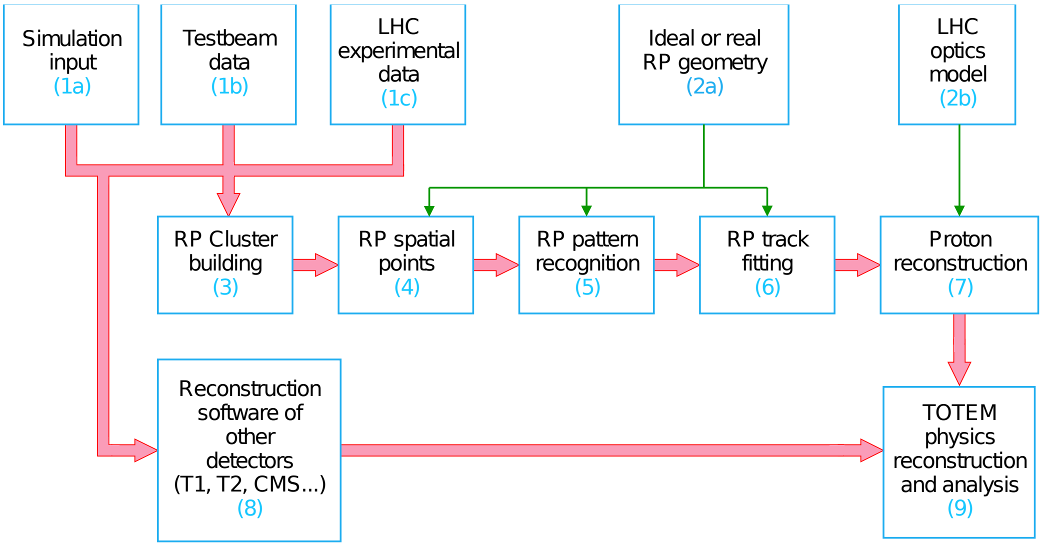

Figure 4.6: Work flow diagram of the TOTEM Roman Pot reconstruction software.

The input data (events) for the reconstruction can come either from simulation (1a) or from real data collected from TOTEM detectors during LHC operation (1b,c). The RP modules of the reconstruction software can interface not only with those for other TOTEM detectors (T1, T2), but also with any reconstruction module in the CMSSW framework (8), as long as the necessary input data is provided. Detector geometry (2a) is the second essential input. Two versions of the geometry may be used: ideal, corresponding directly to the designs, and real, with added displacements as measured after the installation of the physical detectors. The geometry is used at various stages of the following RP local track reconstruction.

Proton tracks in the Roman Pot devices are calculated based on the hits found in the input data. The strip hits are combined into clusters (3) and then, taking into account the geometry, into spatial points (4). Track candidates are then built (5) from these points and the Road Search algorithm is employed to select tracks which are nearly parallel to the beam from the candidates. Next, the accepted tracks are fitted with straight lines (6), producing data for the global proton kinematics reconstruction (7).

This part of the software calculates kinematic parameters of the protons, based on the fitted tracks, accomodating different LHC running scenarios and making use of the parametrisation of the proton transport through the LHC (2b). For example, with low-β^* optics only the RP220 stations will be used. High-β^* runs, on the other hand, will take place with and without the RP147 station enabled. For different physics events, either a single proton (SD event) or a two protons (elastic scattering or DPE) originating from a common point can be reconstructed. Moreover, since the TOTEM experiment is interested in using the information about the transverse position of the collision vertex from the CMS central detector, especially for the high-β^* optics when the beams are 220 - 454 μm wide, there is an option to read that information from the event data. Different centre-of-mass energies for the collisions are also supported (since early LHC runs are done with reduced energies).

Finally, the physics reconstruction, analysis and validation packages (9) are executed. Their task is the reconstruction of physical quantities like the central mass of a DPE event or building histograms and other plots for validation of the reconstructed values. This group of packages also implements the physics analysis capable of using the available information from all detectors of the TOTEM experiment.

4.2.1 Event pattern recognition

The pattern recognition routines perform clusterisation on the reconstructed points on the detectors in a given Roman Pot and detect those, which belong to a common track, saving them as candidates. As the longitudinal angles at which the protons arrive at the Roman Pots usually do not exceed 1mrad, it is enough to accept only the tracks almost parallel to the beam axis. All the others can be safely rejected as background.

Piled-up tracks pose a challenge for the current silicon detector design. Since the detectors in the Pots provide only two strip directions, hits from multiple tracks cannot be easily distinguished and are currently discarded by the current implementation [44]. That is, if in each of the two directions exactly one straight track traversing at least 3 detectors is found, that track is accepted.

4.2.2 Kinematics reconstruction

After an elastic or diffractive scattering event, the leading protons have very small divergence (10 - 150 μrad) and equally small fractional momentum loss $\xi = \frac{\Delta p}{p} = 10^{-7}$ - 0.1. Moving nearly at the edge of the beam, they can be detected in the Roman Pot detectors on both sides of the interaction points only if their transverse position at the Roman Pot stations is large enough to put them on a path traversing the detectors.

As mentioned before in Section 2.2.2, the displacement $(x(s), y(s))$ of a proton at a distance s from the IP is related, via the optical functions L, v, D, to its origin (x^*, y^*, z^*), its scattering angles $\Theta^*_{x,y}$ and the ξ value at the IP. The optical functions shaping the trajectory of the particle through the magnetic lattice, depend on the position along the beam pipe (i.e. on all magnets passed before arriving at that position) but also, due to their nonlinearity, on the particle parameters at the interaction point [16]. The proton reconstruction routines use parameterisations of the optical functions generated by the MAD-X [5] software for each optics configuration, taking into account their slight dependency on the kinematic variables, $\Theta^*_{x,y}$ and ξ.

4.3 Detector geometry in reconstruction

The reconstruction software, similar to the simulation software, can utilize either ideal geometry or real geometry, with measured displacements and rotations included. The ideal geometry, used in the reconstruction of in a non-displaced detector system, contains the design positions of the Roman Pots and their elements, based on the technical documentation as well as the ideal positions of the Roman Pot detectors with respect to the beam. The real Roman Pot detectors have slight shifts and rotations and the beam position at the location of the Pots is also slightly different from the design. Such differences have an effect on the results of the reconstruction. Their values can come either from the simulation stage or from measurements of the physical devices and from alignment procedures, which must be run before physics reconstruction. Without that, the physics results will not accurately reflect reality and might be useless. The Roman Pot alignment procedures make use of both the track reconstruction in the Roman Pot stations and the physics reconstruction. Real geometry data includes the obtained displacements and rotations of the sensitive detectors and the displacements of the beams at Roman Pot locations.

The sharing of the collected charge between detector strips may cause even hits belonging to nearly parallel tracks to appear in adjacent strips of a detector. The clusterisation procedure converts these adjacent hits to a single cluster point and its position is calculated as the centre of the hit group. Cuts on the number of strips per cluster as well as on the number of clusters per detector can be set in a configuration file. The positions of the clusters must be converted from local to global coordinate system before executing the track reconstruction routines, because the fitting operates on global coordinates.

Information about the position and the rotation of each detector is provided by the geometry. It is assumed that each silicon detector is orthogonal to the direction of the beam, but in case of any additional rotation in the longitudinal plane, the detector frame gets projected onto the (x, y)-plane, perpendicular to the direction of the beam. The cluster position (red line in

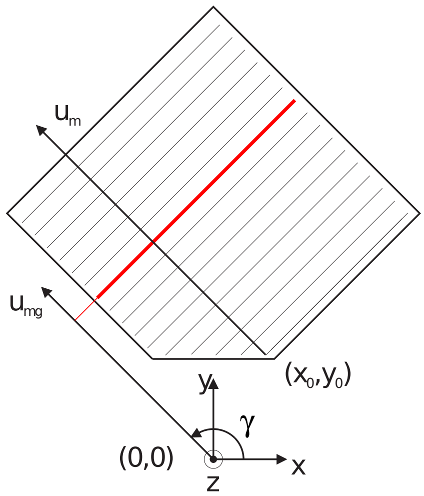

Figure 4.7: A cluster on a detector, seen in local and global coordinate systems. The cluster is shown as a red line. u_m denotes its local and u_{mg} its global position. The x and y coordinates are perpendicular to the beam direction z. The angle γ is the rotation of the silicon detector readout direction with respect to the x-axis of the global coordinate system. (x_0, y_0) are the global coordinates of the local detector frame.

Figure 4.7), is expressed by a three dimensional point (u_{mg}, γ, z), where u_{mg} is the distance between the beam centre and the cluster position, γ is the rotation of the detector and z is the position of the detector along the beam pipe. The reconstruction routines receive the exact values of γ and z from the geometry input.

Chapter 5

Roman Pot detectors geometry

TOTEM's software relies on the computer model of its detectors for physics processes simulation and reconstruction and analysis based on both simulated and real data. In Geant4 part of the software, some physics processes are simulated to happen at the boundaries between elements of the modelled detectors and in the reconstruction part of the software, the geometry is used to determine the exact location of the hits in detectors relative to the beam. Precision and accuracy of the model affects the results of both the simulation and the analysis directly. Therefore, detailed modelling of TOTEM machinery, especially of the detectors and their immediate surroundings is vital to achieving correct results.

Since TOTEM software is developed as an overlay on top of CMS software and uses Geant4 for physics process simulations, the machine and detector geometry models had to be done using the XML-based Detector Description Language (DDL) [31], developed for CMS. While building the models, the Iguana CMSSW Visualisation software [42] was used.

Construction of the computer model of the Roman Pot detector system started with the analysis of the technical drawings describing the components and the elements of the Roman Pots, their placement and their materials.

DDL and Geant4 allow geometry modelling in terms of simple shapes (Figure 5.1, left) and their combinations using boolean operations (Figure 5.1, right), i.e. Constructive Solid Geometry [43]. Additionally, the active (charge collecting) elements need to be marked as "sensitive" in the geometry for the software to record the hit information needed to simulate the digital detector response.

With that in mind, the drawings were analysed and for each independent element of the Roman Pot a decomposition was performed, finding a possible combination of simple solids, which would form the desired shape when put together. For example, the PCB board was modelled as a thin rectilinear

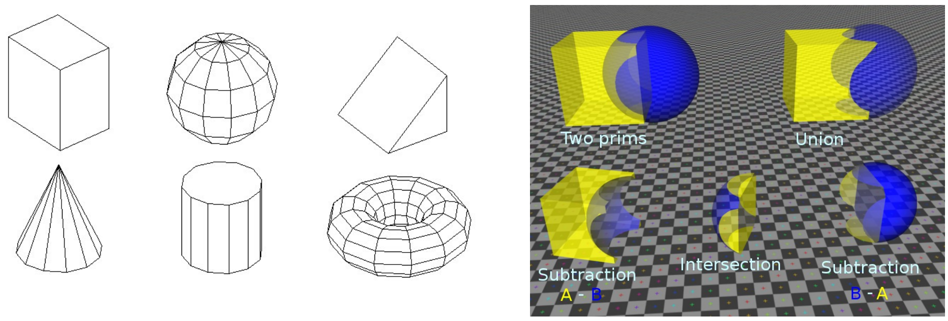

Figure 5.1: Left: basic shapes (solid primitives) of Constructive Solid Geometry: box, sphere, triangular prism, cone, cylinder, torus. Right: basic boolean operations of Constructive Solid Geometry: union, subtraction and intersection.

box with a hole made by subtracting another thin box rotated by 45 degrees from it.

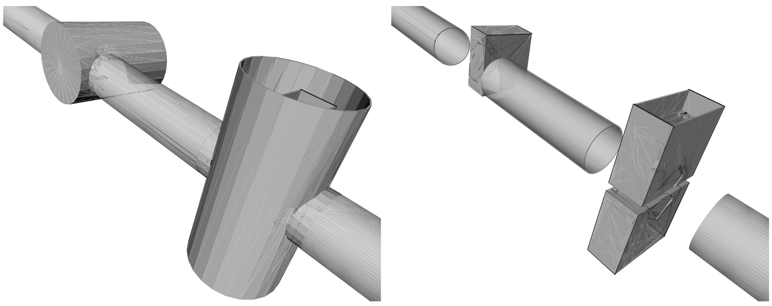

Figure 5.2: Half of the Roman Pot station at 220 m, horizontal and vertical pots inside their vacuum chambers (left), and with the vacuum chambers removed (right)

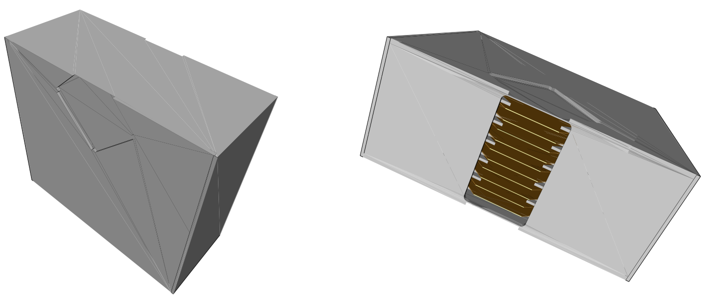

Figure 5.3: Roman Pot box (left) and with the bottom foil removed (right)

Simplified models for the large structures, like the Roman Pot stations assembly and the beam pipe fragments in them (figure 5.2) were created to house the detector models. The large structure models require little precision, because the protons do not pass through their bulk and thus there are no interactions. The last missing component was the Roman Pot box itself (figure 5.3). Since the placements and the positions of the boxes were known, it was enough to create the model of one box and then insert its copies in the appropriate locations (rotated, where necessary) using DDL language PosPart elements.

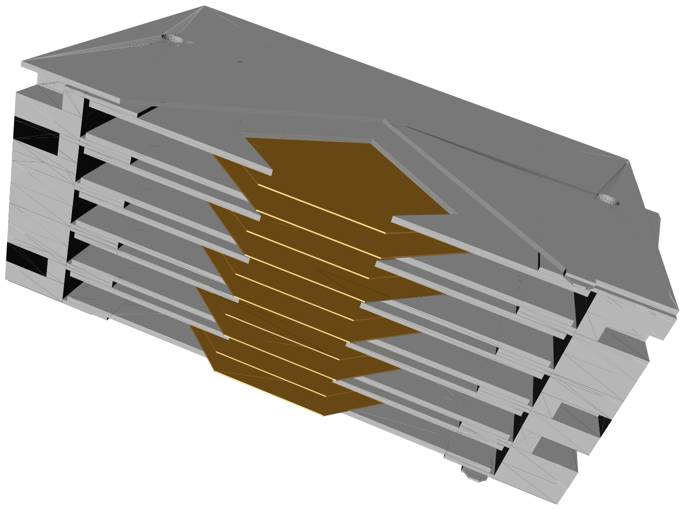

Figure 5.4: Roman Pot detector package

The next step was filling the empty Roman Pot boxes with models of the detector packages (figure 5.4), which consisted of the silicon detectors themselves, glued to their respective PCB boards and their support elements: barrettes on the sides and front and back frames. Again, it was usually sufficient to model just one element of each type and replicate it in the correct positions using DDL. Construction was further simplified by defining common sub-elements and re-using them for building elements which were not simple rotated copies of themselves (for example front and back frames).

With all major elements in place, the models were then made more accurate (for example, support frames models were refined by adding legs and positioning struts to them) in the areas surrounding the sensitive elements, in order to improve the analysis of particles produced by interactions with the materials of the adjacent passive elements. Unfortunately, further improvement of the models was hampered by the instability of the visualisation software and all attempts at making the models more detailed, for example by making some cuts rounded, ended with the software crashing, making visual inspection impossible.

Placement and positioning of the elements with respect to each other was visually verified after modelling the bolt holes on their models. The holes were placed far enough from the detectors for their presence to be irrelevant to the results of the simulation and the reconstruction. However, many distances on the drawings were given relative the holes, thus making them an useful verification tool. Owing to their presence, some inconsistencies in the technical drawings were discovered and corrected after acquiring the latest versions of the relevant drawings.

Finally, an analyser plugin for the TOTEM software framework was written in order to numerically verify the positions of the silicon detectors with respect to the thin foil at the bottom of the Roman Pots. In Geant4 geometry, objects are positioned by rotating around their geometrical centre and translating it with respect to the geometrical centre of the parent object. The analyser code extracts the position of the centre of each pot and calculates the global position of the bottom surface of the pot. A similar procedure is repeated for the beam-facing edge of each silicon detector and the position vectors are subtracted. The calculated position difference is $200\,\mu$m, which is exactly the distance according to the design drawings.

5.1 Hierarchy of volumes

As described in 3.2, Geant4's geometry model is a hierarchy of non-intersecting volumes arranged into an acyclic directed graph. Figure 5.5 shows TOTEM experiment's volume hierarchy, which consists of the IP5 hall, the four stations (two on each side of the IP5 hall: one at 147 m and one at 220 m from the interaction point) and the connecting beam pipes to provide continuity of particle movement simulation. In each station, separately modelled short beam pipe fragments start where the proton transport parametrisation stops and where tracking of particle movement is handed over back to Geant4 in the software. The vacuum chambers of Roman Pot insertions intersecting with the beam pipe are modelled with cylindrical volumes, which, in turn, contain the Roman Pot boxes themselves. The volume of each Pot box is divided into an outer volume containing the vertical walls and the bottom foil, and the inner volume encompassing the detector package and the bottom wall.

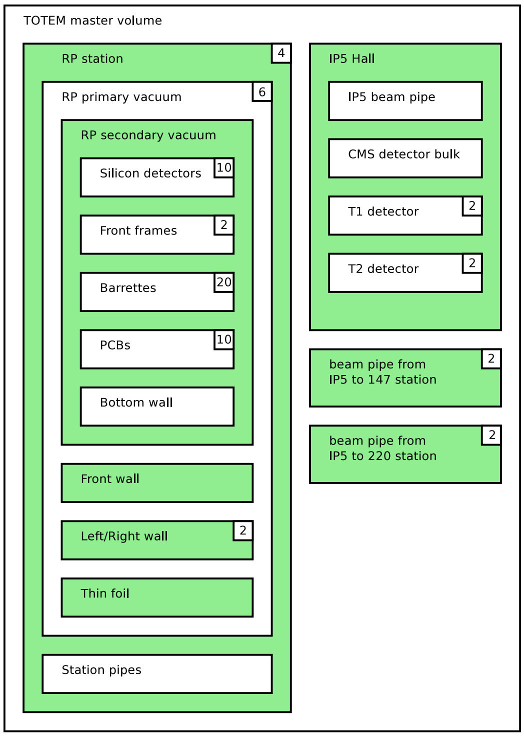

Figure 5.5: The hierarchy of volumes for Geant4 simulations of TOTEM experiment. Some irrelevant components have been omitted for clarity. The numbers in the corners signify the numbers of copies of each component.

5.2 CSG construction

Figure 5.6 shows the key elements of the Roman Pot box.

The silicon detector (a) is constructed by rotating a rectangular box by 45 degrees and cutting off the bottom edge.

The PCB (b) is constructed from a rectangular box by cutting a hole similar in shape to the silicon detector, but slightly smaller.

The side supports (barrettes) (c) are constructed from a union of two rectangular boxes. The bolt holes are created by subtracting a small cylinder from the thicker box.

The front and back support frames (d) are slightly more complicated. Their base is a rectangular box, with a subtracted rectangular box rotated by 45 degrees forming the bottom hole. The legs are made of a union of a box and a trapezoid, while the struts on the side consist of trapezoids from which rectangular boxes are subtracted.

The Roman Pot box (e) is a simple rectangular box with 2 mm thick walls. However, the front and back walls have thinner sections at the bottom,

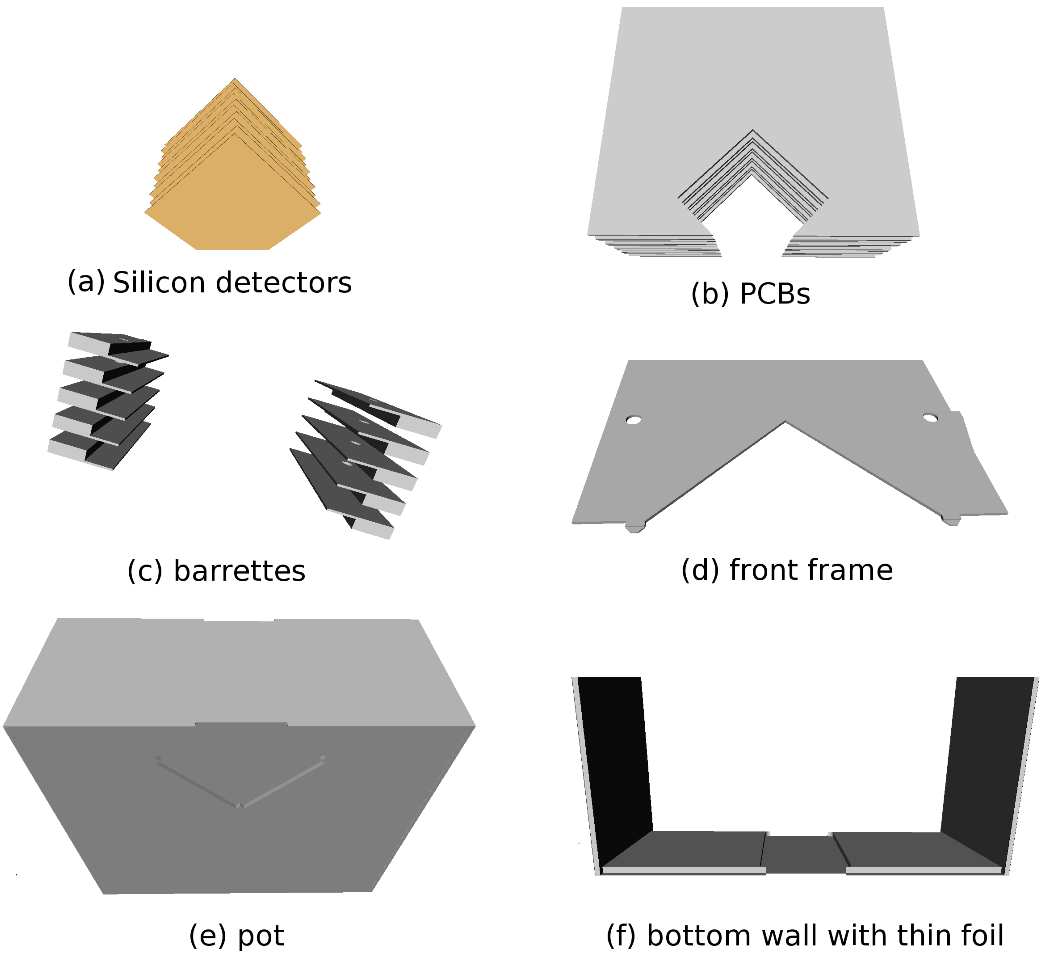

(a) Silicon detectors (b) PCBs (c) barrettes (d) front frame (e) pot (f) bottom wall with thin foil

Figure 5.6: Key elements of the Roman Pot box as used in geometry construction. Visualisation was performed with IGUANA software.

shaped like the silicon detector and constructed in the same way as the holes in the PCBs. The bottom wall (f) has a rectangular hole with rounded edges and is covered by the thin foil - a thin rectangular box with small rectangular cuts along the middle, which forms the thin window at the bottom of the Pot.

Each Roman Pot station, in turn, consists of six Roman Pot boxes enclosed in cylindrical vacuum chambers and connected with beam pipes. The vacuum chambers have holes created by subtracting cylinders with cross-section identical to the beam pipes from them. The six Roman Pot boxes in each station are arranged into two groups consisting of three Pots. Two are positioned vertically, with their thin windows facing the middle of the beam pipe from both directions and the third is positioned horizontally, with its thin window approaching the beam location from the side.

5.3 Materials definition

Exact material definition for each volume and the solids it encloses is essential for correct simulation of particle-matter interactions, that is why great care was taken to obtain detailed descriptions and element compositions of the materials used in the actual construction of the Roman Pot detector systems. The following table lists the names of the materials used.

Component	Material
Vacuum chambers	AISI-316L stainless steel
Pots	AISI-316L stainless steel
PCBs	copper on polyimide substrate (DuPont Kapton E)
Frames	AISI-316L stainless steel
Barrettes	CE7 controlled expansion alloy
Detectors	Silicon

The materials are defined by their density and their base element compositions.

Material	Density	Element composition
AISI-316L stainless steel	$8g/cm^3$	Fe(64.395%), Cr(18%), Ni(12%), Mo(2.5%), Mn(2%), Si(1%), P(0.045%), C(0.03%), S(0.03%)
CE7 controlled expansion alloy	$2.44g/cm^3$	Si(70%), Al(30%)

Chapter 6

TOTEM offline software validation

Validation of the proton reconstruction with the new geometry was performed using the software described in Chapter 4 for an early LHC running configuration with $\beta^* = 2$m optics. Ideal geometry and machine optics were used for simulation of the events. The analysis of the reconstruction results is presented below.

6.1 Acceptance in Roman Pot detector stations

The configuration LHC optics parameters has significant influence on the acceptance of elastically or diffractively scattered protons at the Roman Pots. Figure 6.1 shows the differences in acceptance for different optics configurations. The $\beta^* = 1535$m optics configuration (blue lines), devised specifically for TOTEM is especially useful for detecting elastically scattered protons with very low $|t|$-values (which is essential for extrapolation to $t = 0$ needed for total cross-section calculation). Also, it enables detection of diffractively scattered protons in the whole kinematically permitted ξ range. The acceptance of diffractive protons is still independent of their ξ value for the intermediate $\beta^* = 90$m configuration (red lines). However, there is a noticeable decrease in the t-acceptance. At low-β^* (0.5m$\div$2m) high luminosity optics configuration (pink lines), the diffractively scattered protons can be detected in the RP detectors mostly because of their ξ value in the whole t range, while elastically scattered protons are detectable at very large t.

Figure 6.2 (left) illustrates the overlap in the measurement of elastic and central diffraction cross-section for multiple LHC optics settings. Complete

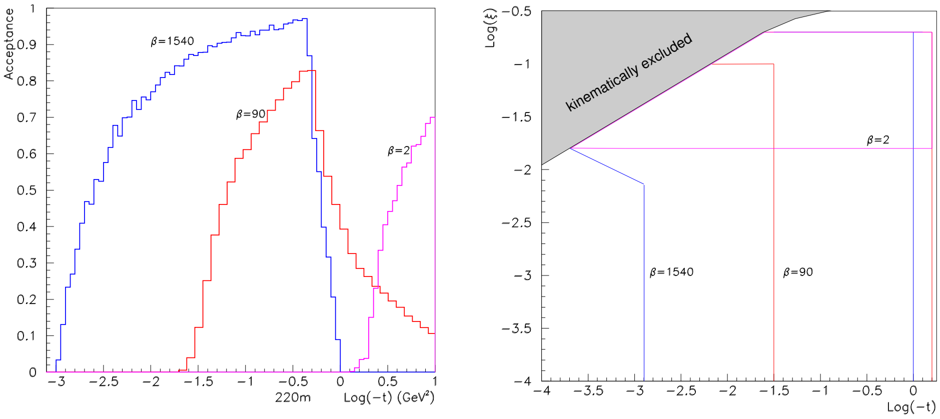

Figure 6.1: Left: acceptance in $log_{10}|t|$ for elastically scattered protons at the Roman Pot station at 220 m for different optics. Right: acceptance in $log_{10}|t|$ and $log_{10}\xi$ for diffractively scattered protons at the same RP station for different optics. The lines indicate 10% level.

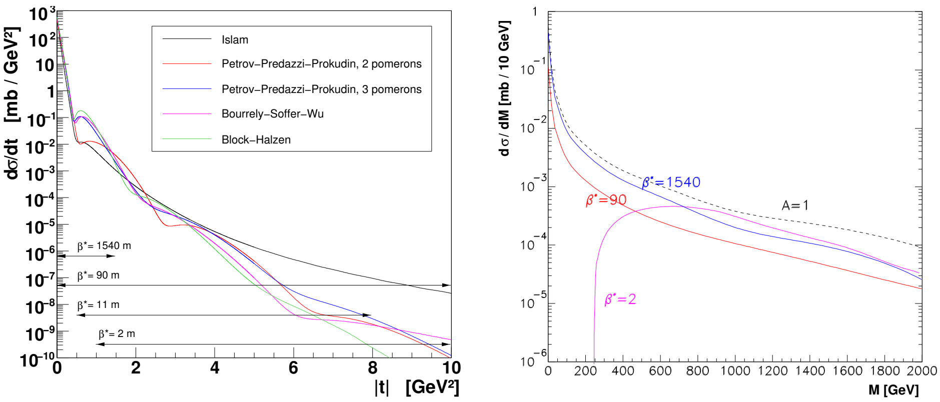

Figure 6.2: Left: differential cross-section of elastic scattering at $\sqrt{s}$ = 14 TeV according to various models. The t-acceptance ranges of different optics configurations are indicated. Right: predicted differential cross-section of central diffraction at $\sqrt{s} = 14$ TeV at different optics configurations (solid lines). Dashed line indicates 100% acceptance.

$2 \cdot 10^{-3} \leq |t| \leq 10\,\mathrm{GeV}^2$ range of elastic events will be covered by running and collecting event data with various optics. Since the planned typical duration of an LHC run is more than a day, the amount of data collected during each run will be enough for accurate reconstruction and calculation of the alignment of the detectors. The overlap between acceptance at the various optics can also be used to verify the results of the measurements

The central diffractive mass distributions (predicted taking into account the acceptance at multiple optics configurations, as well as with full acceptance) are shown in Figure 6.2 (right). For larger masses, the $\beta^* = 2\,\mathrm{m}$ configuration is ideal due to higher luminosity of the beam. For lower masses, both the $\beta^* = 90\,\mathrm{m}$ or the $\beta^* = 1535\,\mathrm{m}$ are useful. Together, they provide good accuracy of the measurement of the differential cross-sections as the function of the central diffractive mass covering the complete range of masses.

6.1.1 Acceptance for $\beta^* = 2\,\mathrm{m}$ optics

Figure 6.3 shows the acceptance of diffractively scattered protons in the RP station at 220 m in t and ξ simulated with $\beta^* = 2\,\mathrm{m}$ optics. Equation 2.23

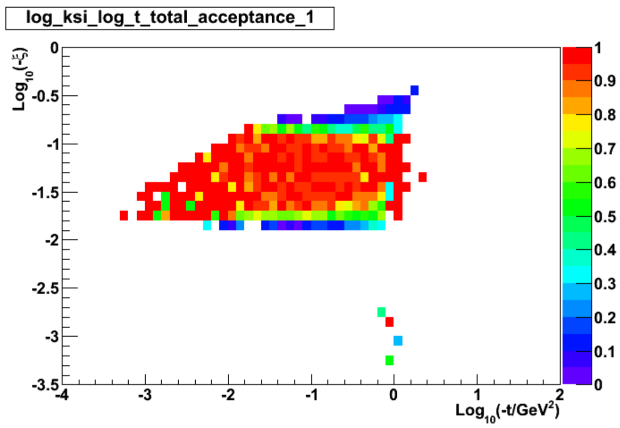

Figure 6.3: Acceptance in t and ξ of diffractively scattered protons at the RP220 station for the $\beta^* = 2\,\mathrm{m}$ optics.

defines the lower bounds of the acceptance in t and ξ. As presented in Table 2.2, the effective vertical length L_y at the Roman Pot station at 220 m is 18 m in the $\beta^* = 2\,\mathrm{m}$ optics. In this configuration, the vertical Pots are located 3.7 mm from the centre of the beam and the lowest detectable angle Θ_y^*[1] is ~ 0.22mrad, which translates into acceptance in t from $0.01\,\mathrm{GeV}^2$. In the horizontal plane, the effective length L_x is 0.49 m, extending the detectable Θ_x^* up to 0.4 mrad. Therefore the t acceptance can reach $\sim 1\,\mathrm{GeV}^2$. As expected, diffractive protons are detectable independently of their momentum loss over the entire ξ range of acceptance.

[1] $\Theta_y^* = K\sqrt{\frac{\varepsilon}{\beta^*}}$, where $\varepsilon = \frac{\varepsilon_N}{\gamma}$, and K is 10-15

6.2 Resolution of the reconstruction of proton kinetic parameters

The calculation of the kinematic parameters $\Theta_{x,y}$ and ξ of the protons emerging from the interaction point is the main task of the reconstruction procedure. Below, the results of the reconstruction for diffractively scattered protons in $\beta^* = 2\,\mathrm{m}$ optics configuration are presented.

The coordinates (x^*, y^*) of the origin vertex of the proton at the IP (see Equation 2.23) are treated as additional free variables due to their contribution to the reconstruction uncertainty, although for low-β^* optics the beam size at the IP is small, so the contribution is less significant than for high-β configuration. The software reconstructs the kinematic variables $(\Theta_x, \Theta_y, x^*, y^*, x)$ by running an inverted χ^2 minimisation procedure [45, 17] on the proton transport equations (2.23).

The obtained values are compared with the ones generated by the simulation and error distribution histograms are produced on that basis. The standard deviation values of these distributions for diffractive protons simulated with $\beta^* = 2\,\mathrm{m}$ optics for various proton kinematics ranges are discussed below.

6.2.1 Resolution of the reconstruction at $\beta^* = 2\,\mathrm{m}$ optics

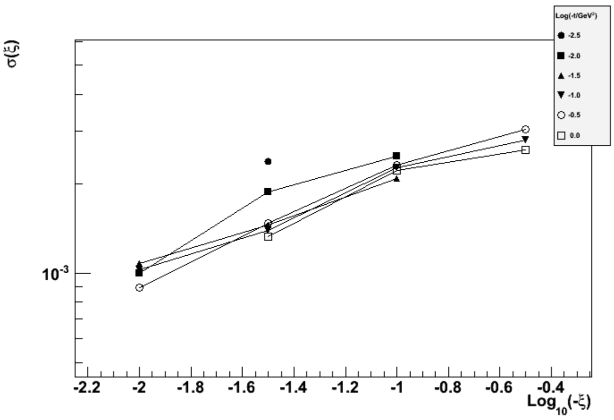

Figure 6.4: ξ-reconstruction resolution of a diffractive proton with $\beta^* = 2\,\mathrm{m}$ optics. Different markers correspond to the resolution at different t-ranges.

Figure 6.4 shows the ξ resolution reconstruction of diffractive protons for different t values. The points in the graph represent values averaged in the range $0.56|\xi_i| \leq |\xi| \leq 1.8|\xi_i|$, where ξ_i is a point in the plot. The ξ-resolution is about 10^{-3}, becoming slightly worse (down to 3×10^{-3}) with rising $|t|$ and $|\xi|$.

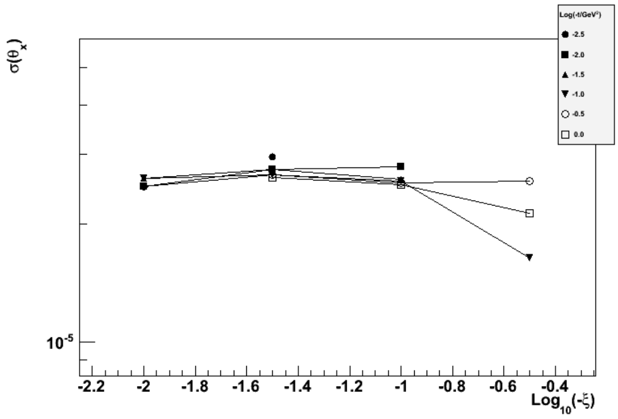

Figure 6.5: Θ_x^*-reconstruction resolution of a diffractive proton with $\beta^* = 2\,\mathrm{m}$ optics. Different markers correspond to the resolution at different t-ranges.

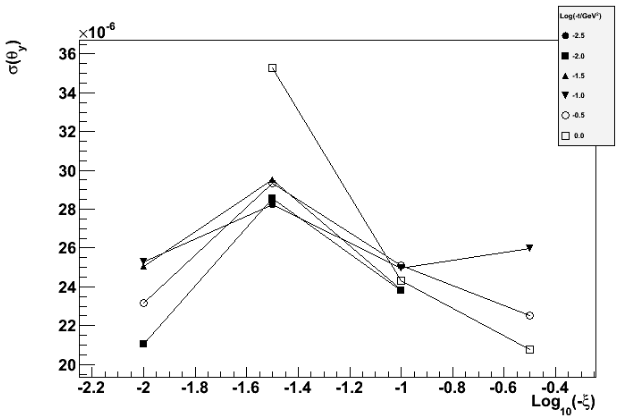

Figure 6.6: Θ_y^*-reconstruction resolution of a diffractive proton with $\beta^* = 2\,\mathrm{m}$ optics. Different markers correspond to the resolution at different t-ranges.

Figures 6.5 and 6.6 show the longitudinal proton scattering angle reconstruction. Since L_x is $0.49\,\mathrm{m}$, the horizontal component of the scattering angle can only be reconstructed with the resolution of $8 \times 10^{-4}\,\mathrm{rad}$, which is two orders of magnitude worse than the beam divergence limit. Fortunately, with L_y equal $18\,\mathrm{m}$ the reconstruction resolution of Θ_y^* is very close to the beam divergence limit of $16\,\mu\mathrm{rad}$.

The reconstruction resolution of Θ^*_x decreases for $|\xi| > 0.1$, whereas the resolution of Θ^*_y varies slightly over the whole $|\xi|$ range. This effect is caused by the machine chromaticity: the optical functions vary with the momentum loss of the proton, which leads to differences in the reconstruction results.

The reconstruction resolution of the four momentum transfer squared $-t \approx p^2\,\Theta^{*2}$ is related to the resolution of the angle $\sigma(\Theta^*)$ by the following:

$$\sigma(t) \approx 2p\sqrt{t}\,\sigma(\Theta^*), \tag{6.1}$$

where p is the momentum of the proton. The longitudinal angular resolutions are similar in the horizontal and in the vertical direction, so in addition to studying the resolutions in $-t_x \approx p^2\,\Theta^{*2}_x$ and in $-t_y \approx p^2\,\Theta^{*2}_y$, $-t \approx p^2\,\Theta^{*2}$ was studied.

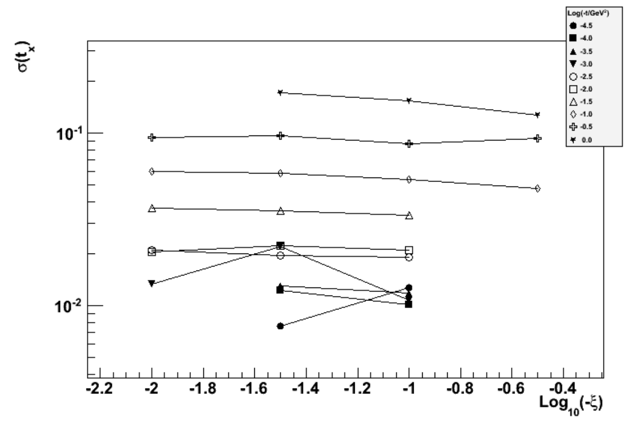

Figure 6.7: t_x-reconstruction resolution of a diffractive proton with $\beta^* = 2\,\mathrm{m}$ optics. Different markers correspond to the resolution at different t_x-ranges.

As seen in Figure 6.7, $\sigma(t_x)$ depends only on t and remains nearly constant throughout the whole $|\xi|$ range, with the exception of $-t \geq 10^{-3}$, improving with the increasing $-t$. The reconstruction gives meaningful physics input when $\sigma(t_x)/t_x < 1$. Based on Figure 6.8, which shows the relative reconstruction errors $\sigma(t_x)/t_x$, we can see that this happens for $-t_x \gtrsim 0.1\,\mathrm{GeV}^2$.

Figure 6.9 shows the obtained reconstruction resolution for t_y. Similar to t_x, it is nearly constant and depends mostly on t, increasing with higher $-t$ values. However, for $-t > 0.1\,\mathrm{GeV}^2$, a dependency on $-\xi$ becomes visible as well. The relative error $\sigma(t_y)/t_y$ is less than 1 only for $-t_y \gtrsim 3 \times 10^{-2}\,\mathrm{GeV}^2$, which can be seen in Figure 6.10.

Total t reconstruction resolution is shown in the Figure 6.11. As expected from the above results, it is also quasi-constant, with its value depending mainly on $-t$ and slightly increasing with higher $-\xi$. The relative error $\sigma(t)/t$

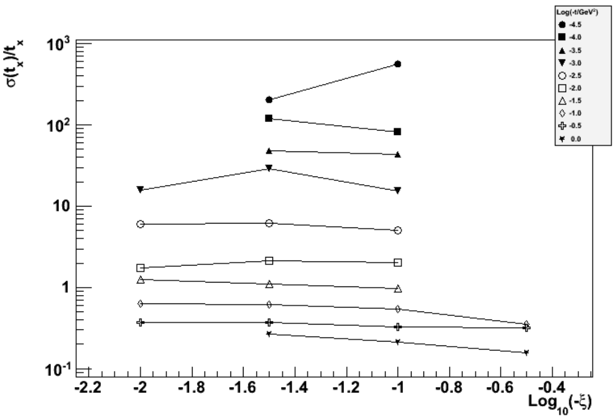

Figure 6.8: Relative error of the t_x-reconstruction of a diffractive proton with $\beta^* = 2\,\mathrm{m}$ optics. Different markers correspond to the resolution at different t_x-ranges.

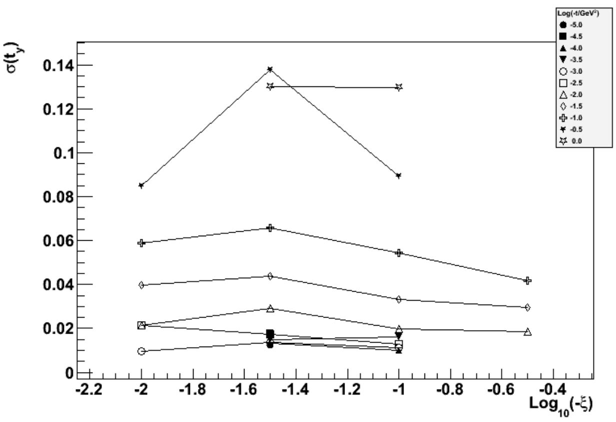

Figure 6.9: t_y-reconstruction resolutions of a diffractive proton with $\beta^* = 2\,\mathrm{m}$ optics. Different markers correspond to the resolution at different t_y-ranges.

shows that usable physics results are available only for $-t \gtrsim 3 \times 10^{-2}\,\mathrm{GeV}^2$, as visible in Figure 6.12.

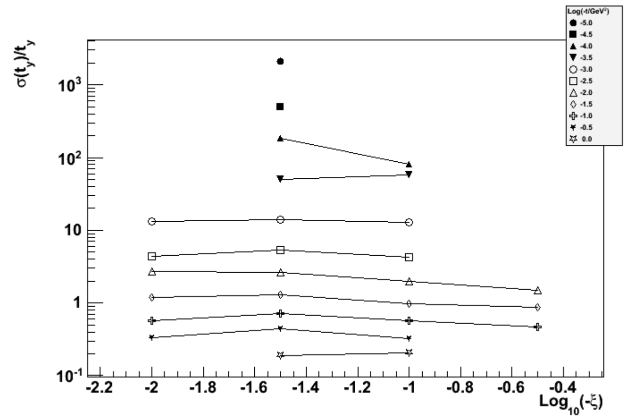

Figure 6.10: Relative error of the t_y-reconstruction of a diffractive proton with $\beta^* = 2\,\mathrm{m}$ optics. Different markers correspond to the resolution at different t_y-ranges.

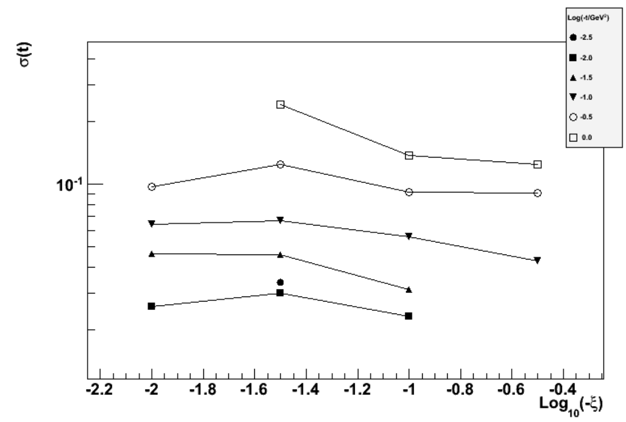

Figure 6.11: Resolution for the t-reconstruction of a diffractive proton with $\beta^* = 2\,\mathrm{m}$ optics. Different markers correspond to the resolution at different t-ranges.

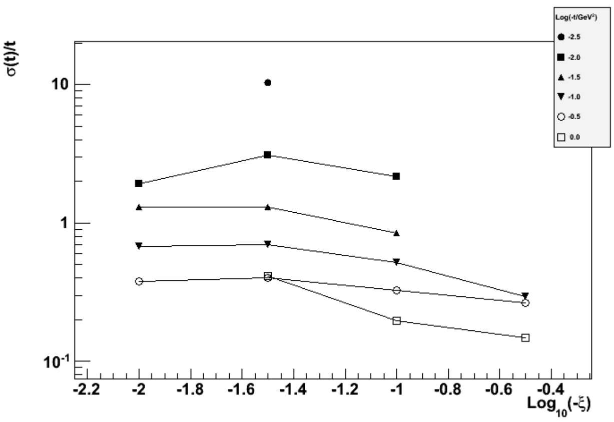

Figure 6.12: Relative error of the t-reconstruction of a diffractive proton with $\beta^* = 2\,\mathrm{m}$ optics. Different markers correspond to the resolution at different t-ranges.

Chapter 7

Conclusions

The Roman Pot detectors are the most important element of the the TOTEM experiment detector set. Complemented by the T1 and T2 telescopes they will be used to measure the total proton-proton cross-section with the luminosity-independent method, and to study proton structure in elastic and diffractive scattering at the LHC.

The modelling of the Roman Pot detectors and the physics reconstruction accuracy of the TOTEM software was studied in detail in this thesis. The simulation software is based on a detailed description of the geometry and of the materials of the Roman Pot stations, which are all defined in a Geant4 compliant way using XML-based Detector Description Language. Based on technical design drawings, a precise geometric model of the Roman Pot detectors has been developed and integrated with the simulation and reconstruction software. The accuracy of the model was numerically verified and shown to match the design drawings with a precision of less than $1\,\mu$m.

The RP simulation and reconstruction software was used to validate the geometry by studying proton acceptance and reconstruction for a selected $\beta^* = 2\,$m scenario. Simulations show that fractional proton momentum loss $\xi = \frac{\Delta p}{p}$ can be reconstructed in the whole ξ-range of acceptance with a precision of $\sigma(\xi) \approx 2 \cdot 10^{-3}$. This optics also exhibits good resolution of the reconstruction of the proton scattering angle. These results are consistent with the theoretical expectations and show the correctness and the accuracy of the detector model.

Bibliography

[1] M. Fowler, "Modern Physics: Relativity and Quantum Mechanics", University of Virginia, 1999.

[2] E. D. Courant and H. S. Snyder, "Theory of the Alternating-Gradient Synchrotron", Annals of Physics 281, 360 408 (2000), 360-408, doi:10.1006/aphy.2000.6012, http://www.idealibrary.com.

[3] E. Wilson, "An Introduction to Particle Accelerators", Oxford University Press, 2006.

[4] H. Bradt, S. Olbert, "Liouville's Theorem", Supplement to Chapter 3 of "Astrophysical Processes", Cambridge University Press, 2008.

[5] MAD-X, http://frs.home.cern.ch/frs/Xdoc/mad-X.html.

[6] TOTEM: Technical Design Report, CERN-LHCC-2004-002, addendum CERN-LHCC-2004-020.

[7] The TOTEM Collaboration, Letter of Intent, CERN/LHCC 9749, LHCC/I11, 1997.

[8] The TOTEM Collaboration, Technical Proposal, CERN/LHCC 997, LHCC/P5, 1999.

[9] R. K. Bock, A.Vasilescu, "Particle Detector BriefBook", Springer-Verlag, 1998.

[10] The CMS and TOTEM diffractive and forward working group: Prospects for Diffractive and Forward Physics at the LHC, CERN/LHCC 2006-039/G-124, 2006.

[11] "A GEM of a detector", CERN Courier, 12/1998

[12] P. Aspell et al., “VFAT2 : A front-end system on chip providing fast trigger information, digitized data storage and formatting for the charge sensitive readout of multi-channel silicon and gas particle detectors”, Proceedings of TWEPP-07, Topical Workshop on Electronics for Particle Physics, Prague, Czech Republic 3-7 September 2007.

[13] Carter et al., REACTION DATA Database: http://durpdg.dur.ac.uk/hep data/react.html

[14] M.M. Islam, R.L. Luddy and A.V. Prokudin, Int. J. Mod. Phys. A21 (2006) 1-41, arXiv:hep-ph/0508200.

[15] D. H. Perkins, “Introduction to High Energy Physics”, 4th ed., Cambridge University Press, 2000.

[16] The TOTEM Collaboration, “The TOTEM Experiment at the LHC”, 2008 JINST 3 S08007, doi: 10.1088/1748-0221/3/08/S08007.

[17] H. Niewiadomski, “Reconstruction of protons in the TOTEM Roman Pot detectors at the LHC”, PhD thesis, 2008.

[18] G. Lutz, “Semiconductor Radiation Detectors”, Springer-Verlag, Heidelberg, 1999.

[19] E.H.M. Heijne, “Muon Flux Measurement with Silicon Detectors in the CERN Neutrino Beams”, Ph. D. Thesis, CERN 83-06, Yellow report (1983).

[20] H. Bichsel, “Passage of charged particles through matter”, AIP Handbook, McGraw-Hill, New York, 1972.

[21] S.M. Sze, “Physics of Semiconductor devices”, 2nd edition, Wiley, New York, 1985.

[22] G. Ruggiero et al.: Planar Edgeless Silicon Detectors for the TOTEM Experiment, IEEE Trans. Nucl. Sci. 52 n5 (2005) 1899.

[23] E. Noschis, “Planar Edgeless Detectors for the TOTEM Experiment at the Large Hadron Collider”, Ph.D. Thesis, University of Helsinki, Helsinki, Finland, 2006.

[24] W.R. Leo, “Techniques for Nuclear and Particle Physics Experiments”, Springer Verlag, 1987.

[25] R.M. Barnet et al., Phys. Rev. D54 (1998).

[26] C. Amsler et al., Phys. Lett B667, 1 (2008), http://pdg.lbl.gov/.

[27] U. Fano, "Penetration of Protons, Alpha Particles, and Mesons", Ann. Rev. of Nucl. Sci., December 1963, Vol. 13, 1-66, (doi: 10.1146/annurev.ns.13.120163.000245).

[28] L. Landau, Journ. Phys. U.S.S.R. 8 (1944) 201.

[29] The CMS Collaboration, "CMS Physics Technical Design Report Volume I: Software and Detector Performance", CERN-LHCC-2006-001.

[30] The CMS Collaboration, "CMS computing: Technical Design Report", CERN-LHCC-2005-023.

[31] M. Case, M. Liendl, F. van Lingen, "XML based Detector Description Language", CMS-NOTE 2005-000.

[32] M.A. Dobbs et al., "Les Houches Guidebook to Monte Carlo Generators for Hadron Collider Physics", Proceedings of "Physics at TeV Colliders", Les Houches, France, May 2003

[33] PHOJET, http://www-ik.fzk.de/∼engel/phojet.html.

[34] PYTHIA, http://home.thep.lu.se/∼torbjorn/Pythia.html.

[35] S. Agostinelli, J. Allison, et al., "Geant4 - a simulation toolkit", Nucl. Instr. and Meth., Vol. 506, Issue 3, July 2003, 250-303.

[36] J. Allison, K. Amako, et al.,"Geant4 Developments and Applications", IEEE Trans. on Nucl. Sci., Vol. 53, No. 1, February 2006.

[37] J. Kaspar, "Influence of smearing effects on the TOTEM experiment", TOTEM-NOTE 2007-005.

[38] V. Talanov, V. Avati, M. Deile, D. Macina, "First results of the machine induced background estimation for the forward physics detectors in the IR5 of the LHC", LHC-PROJECT-NOTE-360.

[39] N. V. Mokhov et al., "Accelerator Related Backgrounds in the LHC Forward Detectors", Proceedings of the Particle Accelerator Conference PAC 2003.

[40] N. V. Mokhov, "The MARS Code System User's Guide", Fermilab-FN-628 (1995); N. V. Mokhov, "Status of MARS Code", Fermilab-Conf-03/053 (2003); http://www-ap.fnal.gov/MARS/.

[41] M. Deile, "Estimates on Machine-Induced Background in the Roman Pots", TOTEM-NOTE 2006-004.

[42] Interactive Graphics for User Analysis, http://iguana.cern.ch/.

[43] Edward Angel, "Interactive Computer Graphics: A Top-Down Approach with OpenGL", Addison Wesley Longman, Inc., 1997.

[44] J. Kaspar, "Reconstruction of elastic events", TOTEM-NOTE 2007-007.

[45] M. Deile, "Algebraic determination of Roman Pot acceptance and resolution for the $\beta^* = 1540$m optics", TOTEM NOTE 2006-002